Ana Rita Gonçalves de Castro

Ciliary recruitment of the dynein-2 motor and its role in *C. elegans* sensory functions

2019/2020

2019/2020

Ciliary recruitment of the dynein-2 motor and its role in *C. elegans* sensory functions

Ana Rita Gonçalves de Castro

Ciliary recruitment of the dynein-2 motor and its role in C. *elegans* sensory functions

Ana Rita Gonçalves de Castro

Ana Rita Gonçalves de Castro

Ciliary recruitment of the dynein-2 motor and its role in *C. elegans* sensory functions

Master in Biomedical Sciences – Diseases Mechanisms

Work Supervised by:

Dr. Tiago J. Dantas, Institute for Research and Innovation in Health (i3S), University of Porto

Dr. Clévio Nóbrega, Centre for Biomedical Research, University of Algarve

2019/2020

Ciliary recruitment of the dynein-2 motor and its role in *C. elegans* sensory functions

Statement of authorship

I hereby declare that I am the author of this work, which is original, and unpublished. Authors and work consulted are properly cited in the text and listed in the references in the required format.

(Ana Rita Gonçalves de Castro)

This work was financed by FEDER - Fundo Europeu de Desenvolvimento Regional funds through the COMPETE 2020 - Operacional Programme for Competitiveness and Internationalisation (POCI), Portugal 2020, and by Portuguese funds through FCT - Fundação para a Ciência e a Tecnologia/Ministério da Ciência, Tecnologia e Ensino Superior in the framework of the project POCI-01-0145-FEDER-029471.

Acknowledgements

A thank you to **Dr. Clévio Nobrega** for the help and clarification of questions I had during the elaboration of my thesis.

I am enormously grateful to my supervisors, **Dr. Tiago J. Dantas** and **Dra. Carla Abreu** for giving me the wonderful opportunity to work with the best team. I am immensely thankful for all the shared knowledge, encouragement, and patience, as well the friendship and support. Since the very beginning have been a source of inspiration to pursue a career in science, and always found time to give their assistance. Thanks for all much-needed advices.

Thanks to my lab mates, **Dr. Bernardo Gama** - "o velhote", **Luísa Fonseca** - "Elsa", and **Tiago Ribeiro** - "Volbeat", for the help in the laboratory, as well the friendship, companionship, and shared laughs. As well the good disposition, that always contributed to a very light and pleasant environment in my daily work.

My thanks to **Diogo Rodrigues** - "Egg Killer", for all the advices and his sharing through all the time I stayed in the laboratory, for all words of friendship and encouragement. Thank you for being by my side and for all the patience to teach me.

I gratefully acknowledge **Dr. Reto Gassman** and **Dr. Jorge Sequeiros**, for helpful advices and for allowing to use some of their equipment.

A heartfelt gratitude goes to **Natacha Batista** – "a mana velhinha", for never letting me down, for helping me when I ask, for your craziness that always makes me smile, for your support and motivation in harder days and for believing in me. Thanks for staying with me and for your contagious joviality and good disposition making my stay in Porto far more pleasant and familiar.

I am grateful to my **father João Batista de Castro** for all the all the support and help provided. My deepest appreciation goes to my nephew **Marco de Castro** for being an inspiration, for help me finding joy in the simple things and for teach me that we can turn weakness into strength. Most importantly, I am eternally grateful to my **sister Maria João Castro** and my **mother Maria Fernanda Gonçalves** who supported me through this opportunity, for always being by me side and for loving me unconditionally. Without you, this thesis would not have been possible. I will be eternally indebted to them, for their immeasurable love and endless support.

Abstract

Cilia are specialized organelles present in most mammalian cells to detect multiple environmental cues, important to regulate cell proliferation, differentiation, and function. Defects in these structures can cause innumerous severe disorders known as ciliopathies.

During ciliogenesis, the ciliary base attaches to the plasma membrane and forms a Transition Zone (TZ) that acts as a specialized ciliary gate. The microtubule-based ciliary axoneme then extends forming the Middle and the Distal Segments, surrounded by a receptor-rich ciliary membrane. Building of all types of cilia depends on the efficient bidirectional transport of different components from the ciliary base and tip, known as Intraflagellar Transport (IFT). Kinesin-II motors transport cargo to the tip, while dynein-2 retrieves signaling molecules and other IFT components to the base. The dynein-2 motor is a large multi-subunit complex composed of several dimers of Heavy Chains (HC), Light Intermediate Chains (LIC), Intermediate Chains (IC) and Light Chains (LC). However, most aspects of dynein-2 subunit recruitment and function are still poorly understood.

To determine the mechanisms that control dynein-2 recruitment and activity inside cilia, and increase our understanding on how mutations in dynein-2 subunits cause developmental ciliopathies, I used live fluorescence microscopy to directly monitor the dynamics of dynein-2 subunits in *Caenorhabditis elegans*.

In this study, I showed the importance of dynein-2 IC (WDR-60) and LIC (XBX-1) for the ciliary recruitment of the dynein-2 HC (CHE-3). I also found that loss of WDR-60 results in severe defects in IFT kinetics and CHE-3 accumulations near the TZ. Strikingly, by disrupting TZ components, I was able to rescue the accumulation of these particles, revealing that, in addition to contributing to dynein-2 activity, WDR-60 is critical for the passage of IFT particles through the TZ to exit cilia. Thus, the results from this study have important implications for the better understanding of WDR60-associated ciliopathies.

Keyword

Ciliopathies, recruitment, dynein-2 complex, Intraflagelar transport, WDR-60, Transition Zone

Resumo

Os cílios são organelos especializados presentes na maioria das células de mamíferos. Os cílios podem ser divididos em dois grupos: móveis e imóveis, de acordo com a sua estrutura e função. Cílios móveis incluem, por exemplo, os flagelos em espermatozoides, importantes para a fertilidade, e os multi-cílios nas células das vias aéreas que promovem o fluxo de muco. Cílios imóveis incluem os cílios dos neurónios olfativos que são responsáveis por captar moléculas odorantes, e os cílios de conexão especializada em fotorreceptores que permite a formação de um segmento externo, critico para a visão. Para além destas funções mais especializadas, os cílios primários presentes na maioria das células contribuem para a regulação da proliferação, diferenciação e função celular. Sendo assim, não é de estranhar que defeitos nestas estruturas podem causar inúmeras doenças severas conhecidas como ciliopatias.

Estas ciliopatias incluem o Síndrome de Bardet-Biedl (SBB), o Síndrome de Joubert (JBTS), a Nefronoftise (NPHP), o Síndrome de Meckel (MKS), a Displasia torácica de costela curta (SRTD), e muitas outras. Apesar da clara importância dos cílios no desenvolvimento humano, ainda não está claro como mutações em diferentes proteínas ciliares podem resultar em múltiplos tipos de patologias com anomalias distintas.

Durante a ciliogénese, o centríolo mais velho do centrossoma (a base ciliar) liga-se à membrana plasmática e forma uma zona de transição que atua como uma porta ciliar especializada - mais precisamente a zona de transição controla as proteínas que podem entrar ou sair do cílio, individualizando-o do citoplasma da célula. O axonema do cílio, formado por microtúbulos, estende-se depois da zona de transição dando origem ao segmento médio e ao segmento distal do cílio, que são envolvidos por uma membrana ciliar rica em recetores. A construção de todos os tipos de cílios depende do transporte bidirecional especializado de diferentes complexos proteicos da base para a ponta do cílio, conhecido como Transporte Intraflagelar (IFT). O IFT depende de proteínas motoras acopladas a complexos de IFT para efetuar o transporte de cargas do cílio. Os motores de cinesina-2 transportam a carga da base até à ponta do cílio, ou seja, no sentido anterógrado, enquanto que a dineína-2 é responsável pelo transporte retrógrado de moléculas de sinalização e outros componentes de IFT para a base do cílio. Os complexos de IFT são compostos de diversas proteínas interligadas entre si que desempenham diferentes funções no IFT, e são divididos em complexo IFT-A e complexo IFT-B. O complexo IFT-A encontrasse mais associado ao transporte retrógrado enquanto que o complexo IFT-B participa no transporte anterógrado sendo essencial para a entrada de componentes para o interior do cílio.

O motor retrógrado da dineína-2 é um grande complexo de múltiplas subunidades composto por vários dímeros de cadeias pesadas (HC), cadeias intermediárias leves (LIC),

cadeias intermediárias (IC) e cadeias leves (LC). Sabe-se que algumas subunidades da dineína-2 são recrutadas para a base ciliar onde são incorporadas nos comboios IFT para depois participarem no transporte retrógrado na ponta do cílio. Alguns estudos sugerem que o recrutamento das subunidades HC e LIC da dineína-2 para dentro do cílio é interdependente. Também foi reportado que a perda de componentes do complexo IFT-B leva ao bloqueio da entrada de algumas subunidades da dineína-2 para o cílio enquanto que a deleção de subunidades do complexo IFT-A tende a reter a subunidades da dineína-2 dentro do cílio. Contudo, a maioria dos aspetos do recrutamento e a função das subunidades da dineína-2 ainda são pouco compreendidos.

Para determinar os mecanismos que controlam o recrutamento e a atividade da dineína-2 dentro dos cílios, e para aumentar a nossa compreensão sobre como mutações nas subunidades da dineína-2 causam ciliopatias de desenvolvimento, neste projeto usei microscopia de fluorescência *in vivo* para monitorizar diretamente a dinâmica das subunidades da dineína-2 em *Caenorhabditis elegans,* na presença e ausência da IC (WDR-60) e LIC (XBX-1).

Os meus resultados revelam a importância da IC (WDR-60) e LIC (XBX-1) no recrutamento e distribuição da dineína-2 HC (CHE-3) dentro dos cílios de neurónios sensoriais. Mais precisamente, confirmei que a subunidade XBX-1 é necessária para CHE-3 ser recrutada para a base ciliar e mostrei pela primeira vez que WDR-60 é dispensável para o recrutamento ciliar de CHE-3 e XBX-1. Contudo, descobri que a perda de WDR-60 resulta em defeitos graves na velocidade e frequência do movimento retrógrado de CHE-3, e em acumulações desta subunidade perto da base do cílio. Em concordância com estes resultados, também observei que a perda de WDR-60 resulta igualmente em acumulações de várias subunidades dos complexos IFT (A e B) ao longo do cílio, com uma redução significativa nas cinéticas dos seus movimentos retrógrados.

Utilizando marcadores da zona de transição do cílio, as acumulações de CHE-3 que observei na ausência de WDR-60 ocorrem na parte mais distal da zona de transição. Com este resultado em consideração, hipotetizámos que a WDR-60 poderia ser importante para a capacidade da dineína-2 de atravessar a zona de transição. Assim, decidimos testar se a remoção dos Y-links da zona de transição seria suficiente para aliviar a acumulação de CHE-3 perto da zona de transição. Efetivamente, quando deletei os componentes da zona de transição que formam os Y-links, consegui reverter as acumulações de CHE-3 mesmo na ausência de WDR-60, revelando que, para além de contribuir para a atividade da dineína-2 durante IFT, a WDR-60 é fundamental para a passagem das partículas de IFT pela zona de transição e assim permitir a sua saída dos cílios.

Com base nos resultados deste estudo, eu proponho 3 possíveis modelos de como a IC WDR-60 poderá estar a influenciar a atividade e funções da dineína-2 e do IFT: i) a IC

WDR-60 é necessária para que o motor da dineína-2 atinja a velocidade/força que necessita para atravessar a densa região da zona de transição; ii) a IC WDR-60 interage com alguma proteína da zona de transição para permitir a passagem da dineína-2 e de componentes do IFT e saída destes do cílio; iii) a IC WDR-60 é necessária para a correta conformação do complexo da dineína-2, consequentemente, influenciando a sua atividade e eficiência em atravessar a zona de transição.

Os resultados deste estudo têm implicações importantes para o melhor entendimento das causas das ciliopatias associadas a mutações em WDR60.

Palavras-Chave

Ciliopatias, recrutamento, complexo dineína-2, Transporte Intraflagelar, WDR-60, Zona de Transição

List of Contents

List of Figures

List of Tables

List of Abbreviations

A

AAA+: ATPases associated with diverse activities

ATP: Adenosine triphosphate

B

B: Base

BBS: Bardet-Biedl syndrome

C

***C. elegans*:** *Caenorhabditis elegans*

CHE: Abnormal Chemotaxis

CHE-3: *C. elegans* dynein Heavy Chain

CEP: CEntrosome-associated Proteins

CT: C-terminus

CRISPR: Clustered Regularly Interspaced Short Palindromic Repeats

D

DNA: Deoxyribonucleic acid

DS: Distal Segment

DYCI-1: *C. elegans* dynein-1 Intermediate Chain

DHC2: Human dynein-2 Heavy Chain

DLC-1: *C. elegans* Light Chain

DYRB-1: *C. elegans* Dynein-1 Roadblock

DYLT-1/2: *C. elegans* Light Chain 1/2

E

***E. coli*:** *Escherichia coli*

EDTA: Ethylenediamine tetra acetic acid

F

FW: Forward

G

GFP: Green Fluorescent Protein

H

HC: Heavy chain

I

IC: Intermediate Chain

IFT: IntraFlagellar Transport

IFT-A: IFT subcomplex A

IFT-B: IFT subcomplex-B

J

JBTS: Joubert Syndrome

K

KAP-1: *C. elegans* Kinesin-II - Associated Protein

KAP3: Human Kinesin-II – Associated Protein

Kbp: Kilo base-pair

KIF: Kinesin superfamily proteins

KIF17: Human Homodimeric kinesin-II

KLP: Kinesin-like protein

KO: Knockout

L

L1-4: Larval stage 1-4

LC: Light chain

LIC: Light intermediate chain

M

MS: Middle Segment

MKS/MKSR: Meckel syndrome / associated proteins

MTs: Microtubules

N

N: N-terminus

N.A: Numerical aperture

N2: Wild Type *C. elegans* strain

NGM: Nematode growth medium

NPHP: Nephronophthisis / associated proteins

O

OSM: Osmotic avoidance abnormal protein

OSM-3: *C. elegans* Homodimeric kinesin-2

P

PCR: Polymerase chain reaction

PHA/B: Phasmid Neurons

PK: Proteinase K

PKD: Polycystic kidney disease

PQR: Posterior Q neuroblast on the right side

R

RB: Roadblock - dynein Light Chain

RFP: Red fluorescent protein

RT: Room temperature

RV: Reverse

S

SRTD: Short-rib thoracic dysplasia

SD: Standard Deviations

T

TAE: Tris-Acetate-EDTA

TCTEX: Human dynein-2 Light Chain

TMEM: Transmembrane protein

TZ: Transition Zone

W

WDR: WD40 related regions of approximately 40 amino acids bracketed by gly-his and trp-asp

WDR34: Human dynein-2 Intermediate Chain

WDR60: Human dynein-2 Intermediate Chain

WDR-60: *C. elegans* dynein-2 Intermediate Chain

WT: Wild type

X

XBX-1: *C. elegans* dynein-2 light intermediate chain **(**X-box promoter motif-containing gene-1)

Chapter 1 - INTRODUCTION

1.1. Cilia

Cilia are specialized sensory and motile organelles present in most mammalian cells to detect multiple environmental cues, important to regulate cell proliferation, differentiation, and function. Consequently, cilia carry out many distinct and critical functions during organ patterning, organ function and fertility [1], which are summarized in **Figure 1.1**.

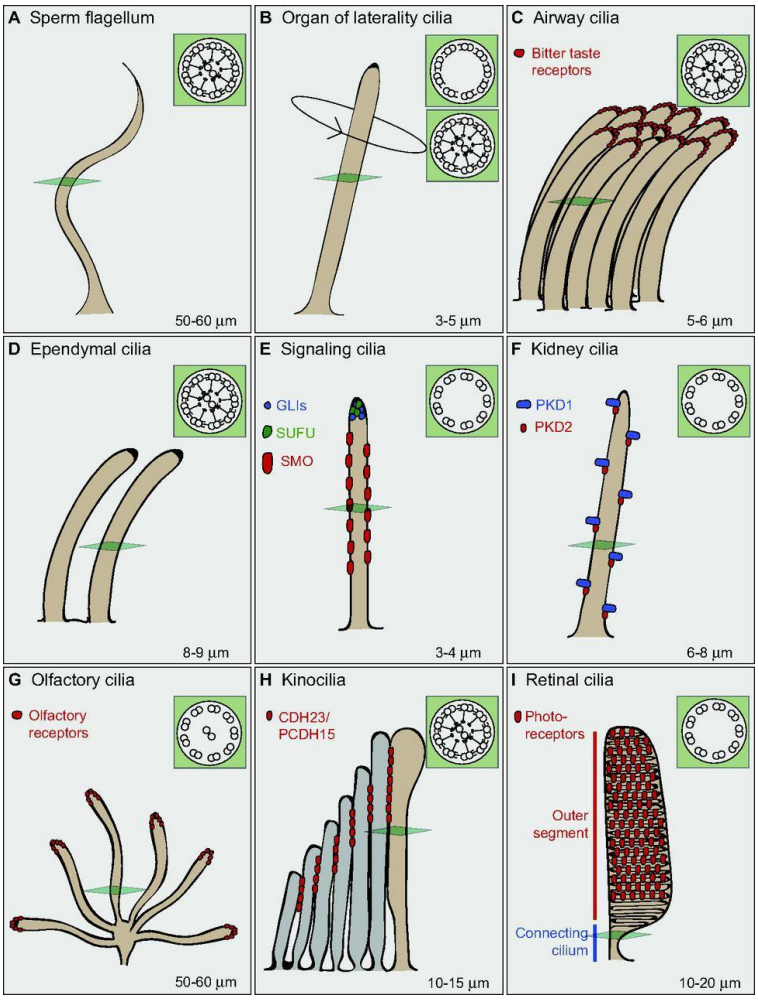

Figure 1.1 – Diversity of cilia types in vertebrates. (A-I) The diversity of cilia that can be found in higher organisms and their range of functions. **(A)** The motile sperm flagellum has a whip-like motion. **(B)** Motile nodal cilia move in a vortical manner to generate a signal gradient and establish left-right asymmetry. **(C)** Motile airway cilia are present in multiciliated epithelial cells. **(D)** Motile cilia in brain ependymal cells function to circulate cerebrospinal fluid. **(E)** Primary or signaling cilium, carries components of the hedgehog and other signaling pathways. **(F)** Renal cilia carry mechanosensory proteins, such as PKD (polycystic kidney disease) and sense urine flow. **(G)** Cilia of olfactory neurons carry olfactory receptors in order to sense odorant molecules. **(H)** The kinocilium serves to polarize the actin-based stereocilia (gray) during development of auditory hair cells. **(I)** The specialized connecting cilium allows the assembly of an outer segment with photoreceptor molecules in retinal cells of the eye. Green inserts represent the axoneme ultrastructure of each cilium type. The average length of each cilium type is given in the bottom right of each panel. Illustration adapted from [2].

It is therefore not surprising that defects in cilia structures and function have been associated with severe disorders known as ciliopathies. These include Bardet-Biedl syndrome (BBS), Joubert syndrome (JBTS), nephronophthisis (NPHP), Meckel syndrome (MKS), short-rib thoracic dysplasia (SRTD), and many others. These disorders can present distinct

abnormalities such as cystic kidneys, obesity, liver disease, skeletal anomalies, *situs inversus* (organ asymmetry defects), and sensory defects (loss of hearing, smell, vision) [3-6]. Despite of the clear importance of cilia in human development, it remains unclear how mutations in different ciliary proteins can result in multiple types of pathologies with distinct abnormalities.

1.2. Cilia Structure and Function

All cilia types are composed of at least three regions: (i) the ciliary base which is attached to the cytoplasmic membrane, (ii) a Transition Zone (TZ) that restricts what enters and exits cilia and (iii) the axoneme which extends from the base protruding to the extracellular environment (**Figure 1.2**). The base is formed from a modified centriolar structure termed 'basal body', made of 9 microtubule-triplets arranged with 9-fold symmetry and attached to the cell membrane through transition fibers. The axoneme is also a microtubule-based structure composed of 9 microtubule-doublets that extend from the base and are surrounded by a ciliary membrane with specialized receptors of signaling pathways. Other ciliary functions such as motility require the presence of an extra pair of central microtubules and specialized axonemal dynein structures that flex cilia to create motion.

The protein and lipid composition of the cilium (membrane and lumen) is physically separated from those of the plasma membrane and cytoplasm, by the TZ that acts as a specialized ciliary gate. The TZ is localized between the axoneme and the basal body, to prevent free diffusion and exclude non-ciliary proteins while allowing the entry of important ciliary proteins [7, 8]. In agreement, several studies have linked proteins normally found in the TZ to a function in regulating ciliary protein composition [9-12]. The TZ is composed of several transmembrane and soluble proteins encoded by three ciliopathy-associated multiprotein modules with different functions: MKS, NPHP, and CEP290 [9, 11, 13]. The MKS and NPHP modules function redundantly in the assembly of Y-link structures, connecting the nine microtubule-doublets to the ciliary membrane [14, 15]. On the other hand, the CEP290 module plays an important role in the formation of the central cylinder [16].

The TZ is followed by the Middle Segment (MS) of the axoneme, characterized by a canonical arrangement of 9 doublet microtubules. At the distal end of the MS, the axoneme converts into the distal segment, consisting of 9 singlet microtubules. The length and ultrastructure of these features may be somewhat divergent in different organisms and in cell types such as in ciliated neurons [17, 18].

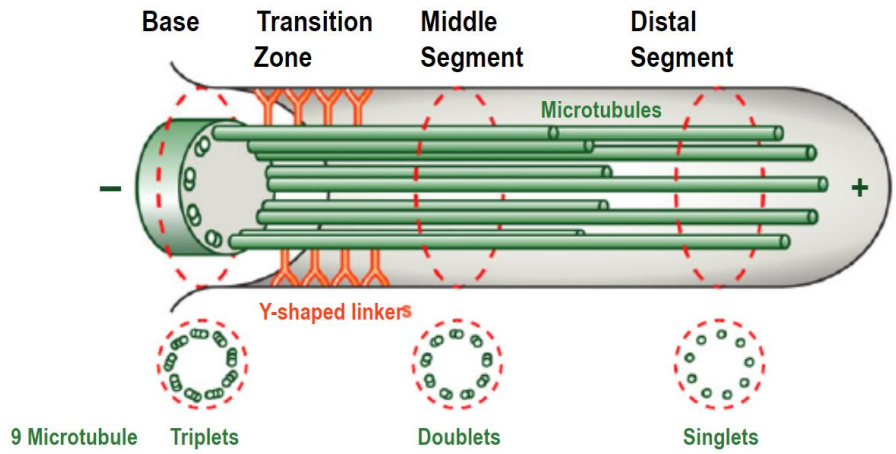

Figure 1.2 – Cilium Structure. Shown is the chemosensory cilium of *C. elegans* neurons. The cilia axoneme is composed of nine pairs of microtubules (green tubules) that extend from a modified centriole named basal body. Four structural and functional cilia domains can be identified, namely the Distal Segment, the Middle Segment, the Transition Zone with the Y-shaped links (orange), and the Base domains. Three most common axonemal architectures: nine microtubule triplets arranged radially at the base, nine doublets arranged radially at the Middle segment and nine microtubule singlets arranged radially at the Distal Segment. The axoneme is the core structural component of the eukaryotic cilium and it assembles by incorporation of precursors such as tubulin subunits onto microtubules plus ends at the distal tips of the axonemes. Adapted from Prevo B. *et al.* (2017) [19].

1.3. Cilia assembly and Intraflagellar Transport

As cilia do not contain any protein synthesis machinery, the assembly and maintenance of cilia rely not only on the appropriate trafficking of proteins within cilia but also on their selective import and export across the ciliary gate.

Ciliogenesis also relies on a specific bidirectional transport of multi-subunit protein complexes called Intraflagellar Transport (IFT). IFT serves to transport different cargos in IFT trains from the ciliary base to the tip of the cilium and along axonemal microtubules. This bidirectional transport of cargos along the axoneme plays essential roles in the assembly, maintenance, and function of cilia [20, 21]. IFT trains are composed of two multi-protein subcomplexes IFT-A / IFT-B, and their movement is powered by motor proteins. IFT trains are assembled at the ciliary base, specifically from the basal body pool [22], and transported along the axoneme by kinesin-2 motors [23]. Upon reaching the tip, these trains are dismounted, rearranged and prepared for the transport in the opposite direction back to the ciliary base by dynein-2 [24-26]. However, the mechanism underlying the assembly of IFT trains at the ciliary base and remodeling at the tip remain unclear (**Figure 1.3**).

The IFT-B complex, composed of sixteen subunits, is essential for ciliogenesis as it mediates ciliary protein trafficking into cilia in the anterograde direction. The kinesin-2 motors that drive anterograde transport are the heterotrimeric KIF3A/B (KLP-20/KLP-11) and KAP3 and the homodimeric KIF17 (OSM-3). These kinesins carry cargoes from the ciliary base to the tip [27]. The IFT-A complex is composed of six subunits that participate in retrograde trafficking, which is driven by the multi-subunit motor protein dynein-2 complex. Dynein-2 and

IFT-A are critical to return the anterograde IFT-machinery, signaling molecules and other turnover products back to the ciliary base [28-31] summarize in **Figure 1.4**.

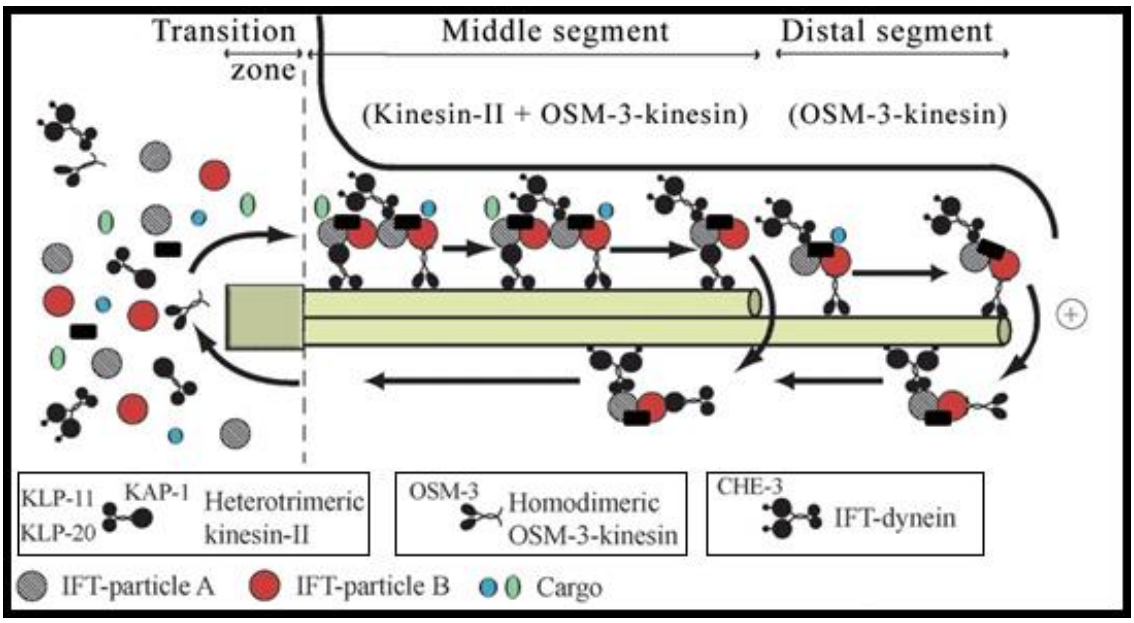

Figure 1.3 – Intraflagellar Transport in *C. elegans*. Components of the IFT machinery and ciliary cargo assemble at the basal body. IFT in *C. elegans* is driven by two distinct types of kinesin-2 motors, heterotrimeric kinesin-II and homodimeric OSM-3, that separately bind IFT particle subcomplexes A and B, respectively, and transport these together with IFT-dynein and cargo along the Middle Segment in the anterograde direction. In the distal segment, OSM-3-kinesin alone transports the IFT particles and dynein/cargo. IFT dynein is activated at the tip of the cilium and provides the retrograde transport, recycling the kinesin-2 motors back to the base. Adapted from Jensen, V.L., *et al*. [32].

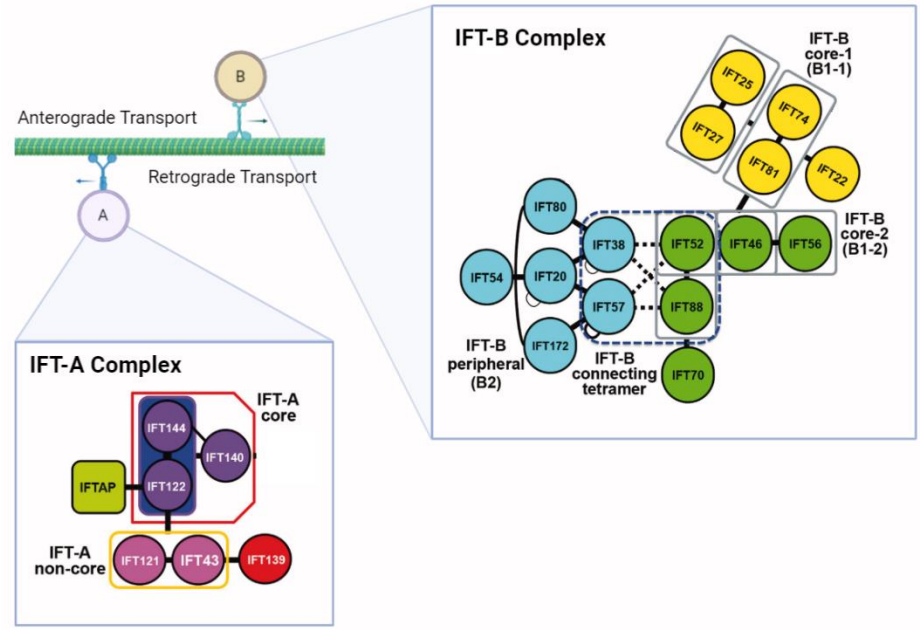

Figure 1.4 – Schematic interaction map of components of the IFT-A / IFT-B. Architectures of the IFT-A and IFT-B complexes and their predicted interaction. The IFT-A complex is composed of six subunits while the IFT-B complex is composed of sixteen subunits. Adapted from Nakayama, K *et al.* (2020) [33].

1.4. The retrograde dynein-2 motor

The dynein-2 motor is a multi-subunit protein complex that is recruited to cilia to function in retrograde transport during IFT. This molecular motor is composed of: a homodimer of Heavy Chains (HC - DHC2 in Humans or CHE-3 in *C. elegans*), each containing a compact N-terminal domain that allows dimerization, an elongated tail region that binds the other complex subunits, and a C-terminal AAA+ motor domain, which is the heart of force generation and microtubule binding that allows for it to move along microtubules; a homodimer of Light Intermediate Chains (LIC in Humans or XBX-1 in *C. elegans*) essential for the stabilization of the Heavy Chains and thus required for all dynein-2 function [34]; a heterodimer of Intermediate Chains (ICs, WDR60 and WDR34 in Humans or WDR-60 and (potentially) DYCI-1 in *C. elegans*), which dimerize with their N-terminus half and bind DHC2 through a β-propeller structure at their C-terminus. Several Light Chains (LCs) bind the dynein-2 ICs to facilitate their heterodimerization (**Figure 1.5**) [35].

Hamada and Tsurumi [35, 36] showed that both dynein-2 ICs were important for the retrograde protein trafficking, in human cells, but their exact function in the dynein-2 complex remains poorly understood.

In Humans, the LCs consist in one Roadblock dimer, three LC8 dimers and one TCTEX−TCTEX1D2 dimer [35].

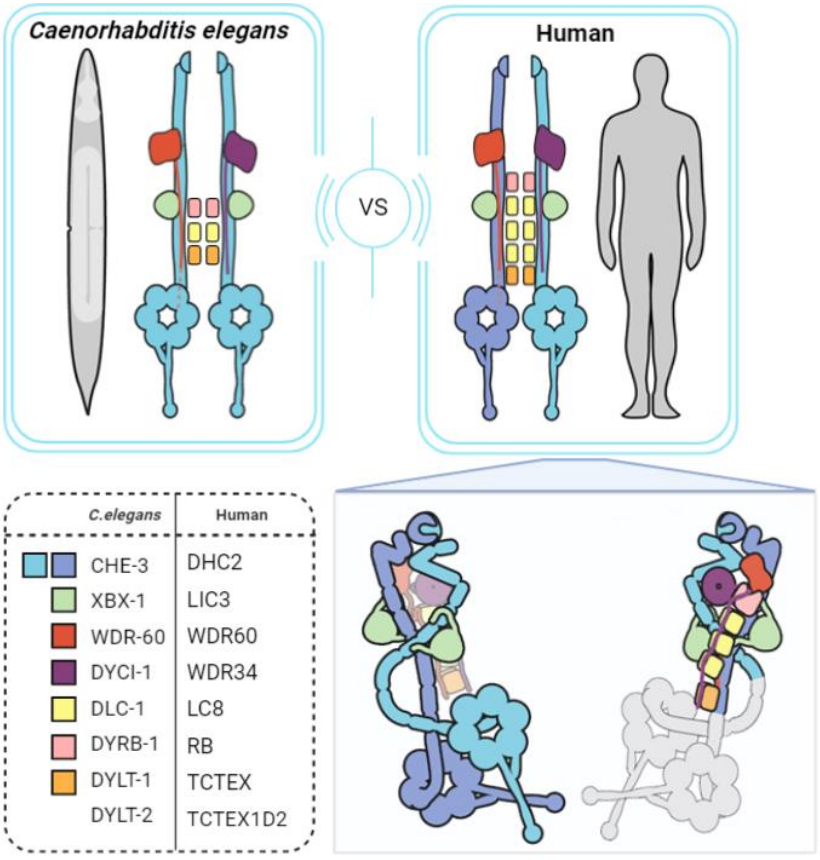

Figure 1.5 – Overview of dynein-2 subunits and their stoichiometry in the structure in *Caenorhabditis elegans* and in humans. Both dynein-2 are composed of two identical Heavy Chains, one heterodimer of

Intermediate Chains, two Light Intermediate Chains, one homodimer of RB and multiples Light Chains. In humans, the two identical copies of the dynein-2 HC are contorted into different conformations by a WDR60−WDR34 heterodimer and a block of two RB and six LC8 LCs. One HC is steered into a zig-zag conformation. Adapted from Toropova, K., *et al.* [37].

1.5. Ciliary recruitment of IFT subunits

A recent study has shown that loss of the dynein-2 LIC (XBX-1) and HC (CHE-3) prevented the recruitment of CHE-3 and XBX-1, respectively, in *C. elegans*, showing that the recruitment of different dynein-2 subunits was interdependent of each other [38]. In addition, the authors reported that loss of IFT88, an IFT-B component, blocked dynein-2 from entering cilia, while deletion of IFT-A subunits (IFT140 and IFT43+IFT139) retained the dynein-2 HC inside cilia.

In humans, it was reported that a golgi protein Giantin and the chaperone NUDCD3 are required for the recruitment of WDR34 to cilia [39, 40]. The same group also showed that WDR34/WDR60 recruitment is interdependent and suggested that it might also interfere with dynein-2 HC and LIC recruitment, although the signals provided by the antibodies were not very clear [40, 41].

Interestingly, anterograde transport in the MS of the cilium, occurs in through the cooperative action of KIF3A/B and KIF17A, carrying the same IFT-particles. Conversely, anterograde transport in the distal segment is exclusively driven by the homodimeric KIF17A. As KIF3A/B are unable to reach the tip of the cilium, they undergo a rapid turnaround event upon reaching the limit of the MS and are redly transported back to the ciliary base by dynein-2. It is believed that, in addition to the axonemal transport during IFT, kinesins and dynein-2 activities are crucial for the entry and exit from cilia through the TZ, but this remains to be demonstrated.

1.6. *Caenorhabditis elegans* as a model system to study sensory cilia in neurons

In *C. elegans*, cilia are found exclusively at dendritic endings of sensory neurons located in the head and tail and are responsible to sense an extensive variety of extracellular and internal signals and mediate a wide spectrum of behaviors. In fact, mutations in genes that control the formation of cilia lead to defects in signaling, food exploration, noxious substance avoidance, chemo-attraction, dauer entry, mechano-sensory and mating behavior. Together with the genetic tools for easy manipulation and the fact that cilia are not essential for *C. elegans* survival, make this a great model system for studying cilia, IFT and cilia-dependent behavior.

Another advantage of this model is that the neuronal network has been completely mapped. Adult Hermaphrodites have 302 neurons, with 60 of them having dendritic endings

that terminate in cilia namely ciliated neurons. The male possesses an additional 48 ciliated neurons (46 in his tail and 4 in his head) [42]. These sensory neurons are essential to detect sensory inputs from the environment, with varieties in structure reflecting diversified sensory functions. [43, 44]). In the head of the hermaphrodite worms, ten chemosensory “amphid channel” cilia contact the external environment through openings in the cuticle and sense hydrophilic molecules to control chemotactic movements. Like the amphid cilia, are sensory cilia located slightly posterior to the anus of the worm and are exposed to the external environment named phasmid cilia (PHA, PHB and PQR) (**Figure 1.6**) [45].

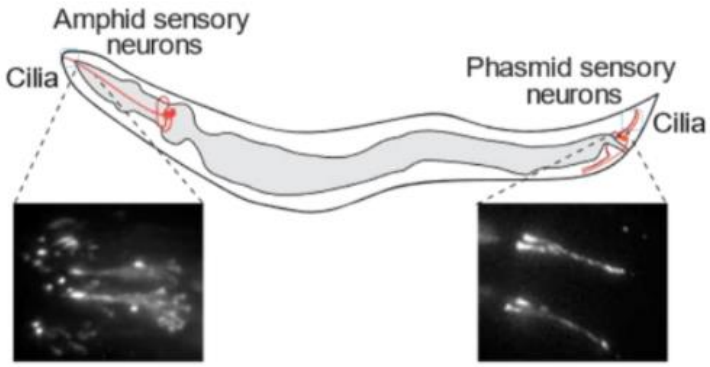

Figure 1.6 - *C. elegans* sensory cilia. In *C. elegans*, cilia are restricted to the dendrites of sensory neurons and are mainly presented in the amphid (head) and phasmid (tail) sensory neurons. Sensory cilia can be visualized by labeling molecules responsible for transport inside cilia, IFT. In this case, cilia were visualized by GFP-labeling of IFT-74, one subunit of the IFT trains.

1.7. Aims of study

The aims of this project are to determine the mechanisms that control the recruitment and activity of dynein-2 inside cilia and to increase our understanding on how mutations in dynein-2 subunits cause developmental ciliopathies.

To address these, I make use of *C. elegans* as an animal model, where cilia are dispensable for survival but are essential for key sensory functions in neurons such as male mating. I use live fluorescence microscopy of knock-in strains with labeled dynein-2 subunits to study their recruitment to cilia when other dynein-2 subunits or IFT proteins are disrupted. I also set out to unravel the contribution of the dynein-2 WDR-60 IC subunit in retrograde IFT. In order to study the contribution of dynein-2-mediated transport in sensory neurons, I then perform behavior assays with dynein-2 mutants. Finally, I also test whether defects in dynein-2 that result in IFT accumulations inside cilia can be corrected by removing the Y-link structures of the TZ.

Chapter 2 – MATERALS AND METHODS

2.1. *C. elegans* growth and maintenance

C. elegans were grown on agar plates containing a lawn of *Escherichia coli* (*E.* coli) OP50 bacteria. This bacteria strain grows slower in NGM plates, which is an advantage for worm's visualization and for worm mating. Instructions for the preparation of NGM can be assessed on WormMethods available on Wormbook.

C. elegans can be maintained at different temperatures (16°C-25°C) for control the rate of animal development. At 16°C, worms have the slowest grown rate, which allows us to maintain them for one week without change them to a new plate. At 25°C, is where worms have the fastest grown rate, however, continual growth at this temperature can cause a lot of stress to them and contribute to the appearance of mutations. In order to maintain strain stocks, worms were transferred from an old plate to a new plate either by picking individual worms with a platinum wire coupled to a Kolle handle or by cutting a chunk of agar and placing it on a new plate. In a week, a single worm can populate an entire plate because *C. elegans* are hermaphrodites and can self-fertilize.

When plates become contaminated with other bacteria or fungi, *C. elegans* cultures were decontaminated by bleaching adult hermaphrodites carrying eggs, with a bleaching solution (5% solution of sodium hypochlorite in 0.5 M NaOH). As only *C. elegans* eggs can survive this treatment, only uncontaminated offspring is born into the new plate.

2.2. Life cycle

The entire life cycle of *C. elegans*, from and egg to an adult hermaphrodite producing more eggs, takes just ~3.5 days at 20°C [46]. *C. elegans* embryogenesis (from fertilization to the hatching) takes approximately 14-16 hours at 20°C. The first few hours, after the fertilization, take place within the mother's uterus, and the embryo is laid outside when it reaches the approximate 30-cell stage [47, 48].

Hermaphrodite embryos, after hatching, become a first stage (L1) larva. The animals begin to eat and develop through four larval stages (L1-L4). Following the L4 stage, adult hermaphrodites begin producing progeny until they have utilized all their self-produced sperm. After the reproductive period, hermaphrodites can live several more weeks before dying of senescence.

When worms grown without food, the development of L2 larvae is arrested, activating an alternative life cycle being namely "dauer" larvae whereby the larva can survive harsh conditions. When dauer larvae are transferred onto plates with bacteria, they continue their development as slightly different L4 larvae [49, 50]. The *C. elegans* life cycle is summarized in **Figure 2.1**.

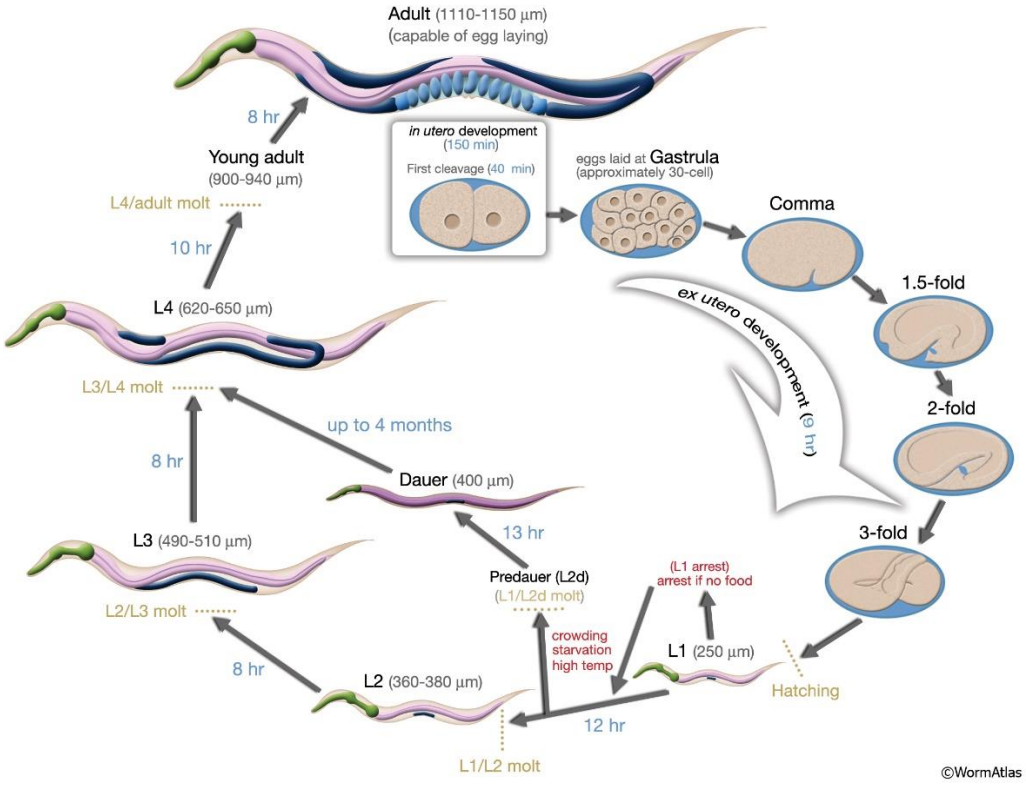

Figure 2.1. *C. elegans* life cycle. *C. elegans* worms have a rapid life cycle that consists of in utero development, four larval stages (L1 to L4) and adult stage. In *C. elegans*, an alternative life cycle pathway – "dauer" – can be activated at L1, in case of unfavorable environment conditions like crowding, starvation and high temperatures. Adapted from WormAtlas [48].

2.3. Freezing *C. elegans*

When a strain is not needed anymore, the worms can be frozen and stocked at -80°C. Generally, 8 plates of recently starved worms (containing mostly L1 stage larvae) were washed with S-basal (100 mM NaCl, 50 mM Potassium Phosphate, pH 6 and 5 mg/L Cholesterol in EtOH) and each strain was collected in a 15 ml falcon tube. Tubes were spun down at 600 g for 3 min, and the supernatant was removed. An equal volume (2ml) of S-basal and worm freezing media (Glycerol 30% (v/v), 50 mM Potassium Phosphate, pH 6, 100 mM NaCl) was used to resuspend worms. 1 ml of worm suspension was added to each cryovial, that were, afterwards, stored on CoolCell containers (Mr Frosty), at -80ºC. After 24 hours, worms were transferred to their final place in the lab stocks, at -80ºC. It is then possible to defrost them many years later.

All strains used in this work and their respective genotype are listed on Table 1.

Table 1: List of strains that were used in this study (name, genotype, and source)

	Name	Source/Made by	*Genotype*
Figure 3.1	GOU2162	Guangshuo Ou lab	*che-3(cas443[gfp::che-3]), I* *xbx-1(cas502[xbx-1::tagRFP::3xFlag]), V*
	TD50	Diogo Rodrigues	*wdr-60 (dan3[wdr-60-linker::3xFlag::GFP]), III* *xbx-1(cas502[xbx-1::tagRFP::3xFlag]), V*
Figure 3.2	TD47	Diogo Rodrigues	*wdr-60 (dan3[wdr-60-linker::3xFlag::GFP]), III*
	TD66	Ana Castro	*che-3(cas443[GFP::che-3]), I* *him-8 (e1489), IV*
Figure 3.3	TD47	**Same as in Figure 3.2**	
	TD81	Diogo Rodrigues	*wdr-60 (dan5[wdr-60(tm6453)::linker::3xFlag::GFP]), III*
	TD73	Diogo Rodrigues	*wdr-60 (dan4[wdr-60Δ1498_4125::linker::3xFlag::GFP]), III*
	TD59	Ana Castro	*wdr-60 (dan3[wdr-60-linker::3xFlag::GFP]), III* *xbx-1(ok279), V*
	TD83	Ana Castro	*wdr-60 (dan4[wdr-60Δ1498_4125::linker::3xFlag::GFP]), III* *xbx-1(ok279), V*
Figure 3.4	GOU2162	**Same as in Figure 3.1**	
	TD40	Diogo Rodrigues	*wdr-60 (tm6453), III* *che-3(cas443[gfp::che-3]), I* *xbx-1(cas502[xbx-1::tagRFP::3xFlag]), V*
	TD49	Diogo Rodrigues	*wdr-60 (dan1[wdr-60Δ1498_4125]), III* *che-3(cas443[gfp::che-3]), I* *xbx-1(cas502[xbx-1::tagRFP::3xFlag]), V*
	TD24	Cármen Vieira	*che-3(cas443[GFP::che-3]) I,* *xbx-1(ok279), V*
Figure 3.5	TD66	**Same as in Figure 3.2**	
	TD86	Ana Castro	*che-3(cas443[GFP::che-3]), I* *wdr-60 (tm6453), III*
	TD48	Diogo Rodrigues	*wdr-60 (dan1[wdr-60Δ1498_4125]), III* *che-3(cas443[GFP::che-3]), I*
Figure 3.6 and 3.7	GOU2362	Guangshuo Ou lab	*ift-74(cas499[ift-74::GFP]), II*
	TD38	Diogo Rodrigues	*wdr-60 (tm6453), III* *ift-74(cas499[ift-74::GFP]), II*
	TD46	Diogo Rodrigues	*wdr-60 (dan1[wdr-60Δ1498_4125]), III* *ift-74(cas499[ift-74::GFP]), II*
	EJP81	Ana Castro	*vuaSi24 [pBP43; Pche-11::che-11::mCherry; cb-unc-119(+)], II* *unc-119(ed3), III* *che-11(tm3433), V*
	TD90	Ana Castro	*wdr-60 (tm6453), III* *che-11(tm3433), V* *vuaSi24 [pBP43; Pche-11::che-11::mCherry; cb-unc-119(+)], II*

	TD119	Ana Castro/Diogo Rodrigues	*wdr-60 (dan1[wdr-60Δ1498_4125]), III* *che-11(tm3433), V* *vuaSi24 [pBP43; Pche-11::che-11::mCherry; cb-unc-119(+)], II*
Figure 3.8	EJP16	Diogo Rodrigues	*vuaSi2 [pBP22; Posm-3::osm-3::mCherry; cb-unc-119(+)], II* *unc-119(ed3), III* *osm-3(p802), IV*
	TD92	Diogo Rodrigues	*wdr-60(tm6453), III* *vuaSi2 [pBP22; Posm-3::osm-3::mCherry; cb-unc-119(+)], II* *osm-3(p802), IV*
	TD127	Ana Castro	*vuaSi1 [pBP20; Pkap-1::kap-1::eGFP; cb-unc-119(+)], IV*
	TD110	Diogo Rodrigues	*wdr-60(tm6453), III* *vuaSi1 [pBP20; Pkap-1::kap-1::eGFP; cb-unc-119(+)], IV*
Figure 3.9	N2	CGC	*WT (ancestral N2 Bristol)*
	TD56	Ana Castro	*him-8 (e1489), IV*
	TD62	Diogo Rodrigues	*him-8 (e1489), IV* *wdr-60 (tm6453), III*
	TD63	Diogo Rodrigues	*him-8 (e1489), IV* *wdr-60 (dan1[wdr-60Δ1498_4125]), III*
	OE3002	OE lab CGC	*him-8 (e1489), IV* *xbx-1(ok279), V*
Figure 3.10	N2	**Same as in Figure 3.9**	
	TD37	Diogo Rodrigues	*wdr-60 (tm6453), III*
	TD45	Diogo Rodrigues	*wdr-60 (dan1[wdr-60Δ1498_4125]), III*
	JT11069	OMRF Knockout Group	*xbx-1(ok279), V*
Figure 3.11	TD96	Ana Castro	*che-3(cas443[GFP::che-3]), I* *vuaSi21 [pBP39; Pmks-6::mks-6::mCherry; cb-unc-119(+)], II*
	TD104	Ana Castro	*che-3(cas443[GFP::che-3]), I* *wdr-60 (tm6453), III* *vuaSi21 [pBP39; Pmks-6::mks-6::mCherry; cb-unc-119(+)], II*
	TD122	Ana Castro/Diogo Rodrigues	*che-3(cas443[GFP::che-3]), I* *wdr-60 (dan1[wdr-60Δ1498_4125]), III* *vuaSi21 [pBP39; Pmks-6::mks-6::mCherry; cb-unc-119(+)], II*
	TD103	Ana Castro	*xbx-1(ok279), V* *vuaSi21 [pBP39; Pmks-6::mks-6::mCherry; cb-unc-119(+)], II*
	OEB730	OEB lab CGC	*oqEx500 [tmem-107:: GFP; unc-122p::DsRed]*
	TD80	Ana Castro	*wdr-60 (tm6453), III* *oqEx500 [tmem-107::GFP; unc-122p::DsRed]* *him-8 (e1489), IV*
	TD60	Diogo Rodrigues	*wdr-60 (dan1[wdr-60Δ1498_4125]), III* *oqEx500 [tmem-107::GFP; unc-122p::DsRed]*
	TD79	Ana Castro	*xbx-1(ok279), V* *oqEx500 [tmem-107::GFP; unc-122p::DsRed]*

Figure 3.12	TD96	**Same as in Figure 3.11**	
	TD104	**Same as in Figure 3.11**	
	TD122	**Same as in Figure 3.11**	
Figure 3.13	TD10	Carla Abreu	*che-3(cas443[GFP::che-3]), I*
	TD86	**Same as in Figure 3.5**	
	TD129	Ana Castro	*che-3(cas443[GFP::che-3]), I* *mksr-2(tm2452) IV*
	TD97	Diogo Rodrigues	*che-3(cas443[GFP::che-3]), I* *mksr-2(tm2452), IV* *nphp-4(tm925), V*
	TD100	Diogo Rodrigues	*wdr-60 (tm6453), III* *che-3(cas443[GFP::che-3]), I* *mksr-2(tm2452), IV*
	TD99	Diogo Rodrigues	*wdr-60 (tm6453), III* *che-3(cas443[gfp::che-3]), I* *mksr-2(tm2452), IV* *nphp-4(tm925), V*

2.4. Genetic Crosses

New strains were generated by crossing two already existing strains. The first strain was crossed with male N2 stocks to generate male progeny that was then used to cross with the hermaphrodites of the second strain (**Figure 2.2** diagram). Strain screening was achieved by performing worm lysis and PCR. A single worm was picked into a PCR tube lid containing 10 µL of lysis mix. To prepare the lysis mix, 5 µL of 20 mg/ml Proteinase K (PK) was added to 95 µL of 1 x PCR lysis buffer (10 mM Tris pH 8, 50 mM KCl and 1.5 mM $MgCl_2$), for a 10 worms' reaction. PCR tubes were, first, incubated at 65ºC for 90 minutes and then, at 95ºC for 15 minutes, as a way of inactivating Proteinase K. Each single worm PCR reaction contained: 3,2 µL ddH2O, 5 µL NZYTaq II 2x Green Master Mix (NZYtech), 0,4 µL forward (FW) and reverse (RV) primers (10 µM) and 1 µL of worm lysis. PCR conditions are described on Table 2.

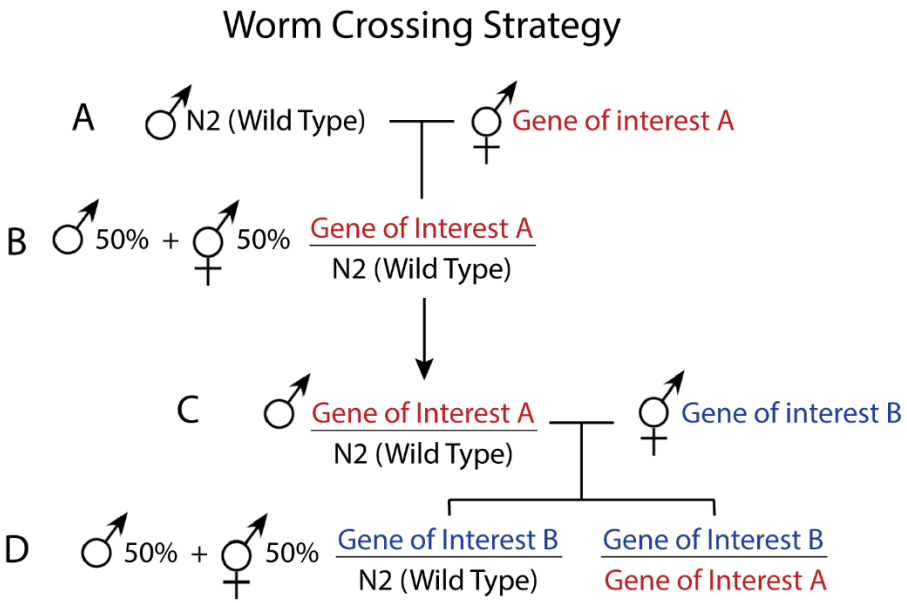

Figure 2.2. Diagram of the general strategy used to cross *C. elegans* strains. (A) The first strain with the gene of interest A (red) was crossed with a Wild Type male to generate both males and hermaphrodites of the gene of interest A. **(B)** Since both strain were homozygous then 100% of the progeny was heterozygous with 50% being males and 50% hermaphrodites **(C)** Males heterozygous of the gene of interest A were crossed with hermaphrodites homozygous of the gene of interest B (blue). **(D)** The progeny was composed of worms only containing the gene of interest B and containing both gene of interest A and B (new strain).

Table 2 – PCR conditions to assess the genotype of new strains. * The annealing temperature was calculated based on the primer T_m and optimized for each pair of primers. A touchdown PCR approach was used, in which the initial annealing temperature is higher than the optimal T_m of the primers and is gradually reduced over sequential cycles.

Step	Temperature	Time	Number of cycles
Initial denaturation	95 ºC	2 min	1
Denaturation	94 ºC	30 s	25-37
Annealing	*	30 s	
Extension	72 ºC	30 s/kbp	
Final extension	72 ºC	5 min	1

PCR primers used in this study, as well as their target genes, are included on Table 3. PCR products were loaded to a 1% agarose gel, containing 1 µL GreenSafe Premium (NZYtech) per 100 mL of 1x TAE buffer (stock 50x TAE buffer contained 2 M of Tris base, 1 M glacial acetic acid, and 50 mM EDTA, pH 8). DNA ladder, NZYDNA Ladder II (NZYtech), was also loaded to the gel, as a way of accurately determine the molecular weight of PCR products. The agarose gel was run at different voltages (100-130V) for 20-30 minutes and then, visualized on Gel Doc XR (Biorad).

Table 3: Primers used in this study and their target genes.

Screen	Primer	Sequence (5' --> 3')	Annealing Temperatures
GFP::CHE-3 knock-in	oTD54 (FW)	ACAGGTGGAGTGTATTTAATGAG	61-51
	oTD2 (RV)	ACAACACGAAAGACGTTGGCTG	
XBX-1::RFP knock-in	oTD3 (FW)	GTTCGACGCCTCGTTGAGAA	60-50
	oTD4 (RV)	CACCAATACAAGTCTAAGCTAG	
IFT-74::GFP knock-in	oTD5 (FW)	CACGAGTATGACTCACAAGGAG	60-50
	oTD6 (RV)	CGGAAAGGGTGCTTCATACTTG	
***xbx-1* (ok279 deletion)**	oTD22 (FW)	AGTTCGTCGGAGACACGAATC	62-56
	oTD23 (RV)	CCACGAACGGCAATTGGTTAC	
WDR-60 **(ΔCT) deletion**	oTD26 (FW)	GAGAGAGGAGAGACAGAAGAGAAAGAG	60-53
	oTD41 (RV)	CAAATGCCACAAGATACGGAC	
WDR-60 knock-in	oTD41 (RV)	CAAATGCCACAAGATACGGAC	62-54
	oTD42 (FW)	TCATAACATACTGGGATTTGGG	
ΔWDR-60 deletion	oTD40 (FW)	AGTTGAGTTGATTTCCTTGGG	60-50
	oTD53 (RV)	GATATGAAACCTGTGTTGCAG	
***nphp-4* (tm925) deletion**	oTD153 (FW)	GCCATTCTTGGATCCGCATA	60-50
	oTD154 (RV)	CCGGCCAGTTGAAATGAAAC	
***mksr-2* (tm2452) deletion**	oTD155 (FW)	TTGCTCATCTCCCTAATGGC	60-50
	oTD156 (RV)	TGGATTCGGTGATAATCGGC	
***kap-1* (ok676) deletion**	oTD157 (FW)	TTTCATTCCTGCCACGTCAC	60-50
	oTD158 (RV)	CTTTGATTGACCCAACTCACC	
***ccep-290* (tm4927) deletion**	oTD159 (FW)	AGCTTGTTCGTCATTTCGGT	60-50
	oTD160 (RV)	CTGTAGGCACAAGGCCATAA	

***che-11* (tm3433) deletion**		oTD161 (FW)	TCTTCGTAGTATCTTGCAGCG	60-50
		oTD162 (RV)	TACAACTTCAAGGAATGCAGC	
Mos II 5'	**knock-in**	oTD270 (FW)	GACATTTGAGAATGGCATTGA	60-50
		oTD271 (RV)	TTTACAAGGACTTGGATAAATTGG	
	Wild Type	oTD272 (FW)	AGGCAGAATGTGAACAAGACTCG	66-56
		oTD273 (RV)	ATCGGGAGGCGAACCTAACTG	
Mos IV 5'	**knock-in**	oRG290 (RV)	TTTACAAGGACTTGGATAAATTGG	60-50
		oTD320 (FW)	CAGGAGAGCAAGGACCAAAG	
	Wild Type	oTD319 (RV)	GCCAAATGCCATAGTCAATGG	60-50

2.5. Fluorescence imaging of cilia

Young adult hermaphrodite worms were anaesthetized with 10mM Levamisol, placed on a 5% agarose pad mounted on a microscope slide and covered with an 18 mm×18 mm coverslip (No. 1.5H, Marienfeld). For the profile of particle distribution along cilia, worms were imaged using an Axio Observer microscope (Zeiss) equipped with 63x, 1.46 NA objective lens, an Orca Flash 4.0 camera (Hamamatsu), controlled by ZEN software (Zeiss). Cilium stacks were acquired at every 0.04 µm during 300 and 800 ms exposure time for GFP and mCherry (respectively).

For kymographs, imaging was performed using an Olympus IX81 (Olympus, UK) inverted microscope coupled to an Andor Revolution XD spinning disk confocal system composed of an iXonEM+ DU-897 with 2x port coupler (ANDOR Technology, UK), a solid-state laser combiner (ALC-UVP 350i, Andor Technology), and a CSU-X1 confocal scanner (Yokogawa Electric Corporation), controlled by Andor IQ3 software (Andor Technology). 200 frames were recorded for each phasmid cilium at 333ms per frame with 40% laser intensity and 300 EM gain. All imaging was performed at 20°C in temperature-controlled rooms kept.

2.6. Image processing and analysis

Z-stack and time-lapse sequences were processed and analyzed with Fiji software (Image J version 2.0.0-rc-56/1.52 p). Intensity distributions were obtained by drawing a line along the cilium, starting at the base to the tip, and a plot profile was generated with the gray values for each pixel within the line. A small area was drawn inside the worm to obtain a

background sample. I used the distribution of different fluorescence markers along cilia to measure the length of the cilia of *wdr-60* mutants in each different background.

Kymographs were generated using KymographClear toolset plugin in ImageJ (http://www.nat.vu.nl/~erwinp/downloads.html). Tracks of individual IFT particles along the whole cilium length were automatically generated by the KymographClear toolset and then manually selected based on their continuity for the retrograde transport. IFT velocities for the anterograde transport at different positions along cilia were automatically extracted in the KymographDirect software (http://www.nat.vu.nl/~erwinp/downloads.html), classified into groups at the distance of every 0.5 µm along cilia and further quantified to generate the velocity curves as in **Figure 2.3(A-D)**. For a rough calculation of velocities at different ciliary subregions, IFT velocities were further grouped into three classes (TZ: 1µm-2µm; MS: 2µm-5µm; DS: 5µm-end) and quantified in **Figure 2.3(D)**. Particles that could not be tracked along the full length of cilia or were not clearly separate were not used for quantifications.

All cilia analyzed were chosen based on their position and orientation, and to ensure the quality of images used for velocity calculation, movies only in stable focal planes that cover the whole cilium structures were used to generate kymographs. At least 15-20 of worms were examined for each strain from three independent experiments.

2.7. Mating Assays

Mating assays were performed as described in Hodgkin, 1983 [51] for quantitative mating efficiency tests. Briefly, six L4 hermaphrodites N2 and six young males of the strain to be tested were placed together on a mating plate (i.e. a 5 cm NGM agar plate with an ~1 cm spot of OP50 seeded at the center of the plate). Note that males were separated 24 hours prior to the experiment and placed on a 5 cm NGM seeded plate at 20°C. The worms were then allowed to mate for 15 and 24 hours at 20°C, after which the hermaphrodites were isolated onto a new 5 cm NGM seeded plate and kept at 20°C for 24 hours to lay eggs. After this period, hermaphrodites were removed and plates with eggs were kept at 25°C. Two days after, the number of total progeny and the number of male progeny on the plate were counted. In order to obtain enough male progeny to be used in these assays, all strains used for mating, except for N2, contained a *him-8* null mutation, which leads to an increase in mis-segregation of the X chromosome during meiosis I [52] and, as a result, an increase in the number of male progeny. Young males N2 and *him-8* were used as positive mating controls while young males mutant for *xbx-1*, previously characterized as cilia- and mating-defective worms [34], were used as a negative control. Note that the mating efficiency of *him-8* males is undistinguishable of those from N2 strain, thus, excluding the possibility that any phenotype seen in the *wdr-60* mutant strains is a result of any contribution from the *him-8* mutation.

2.8. Osmotic Avoidance Assay

Osmotic avoidance assays were performed on an NGM non-seeded plate at room temperature (RT) with five young adult hermaphrodite worms and placed inside of a glycerol (59%) ring. The worm's behavior was immediately monitored for 10 minutes. Worms that left or stayed in the ring for more than 20 seconds were classified as escapers. N2 and Δ*xbx-1* worms were used as positive and negative controls, respectively. Note that the worms being assayed were separated 24 hours before the experiment on an NGM seeded plate and kept at 20°C.

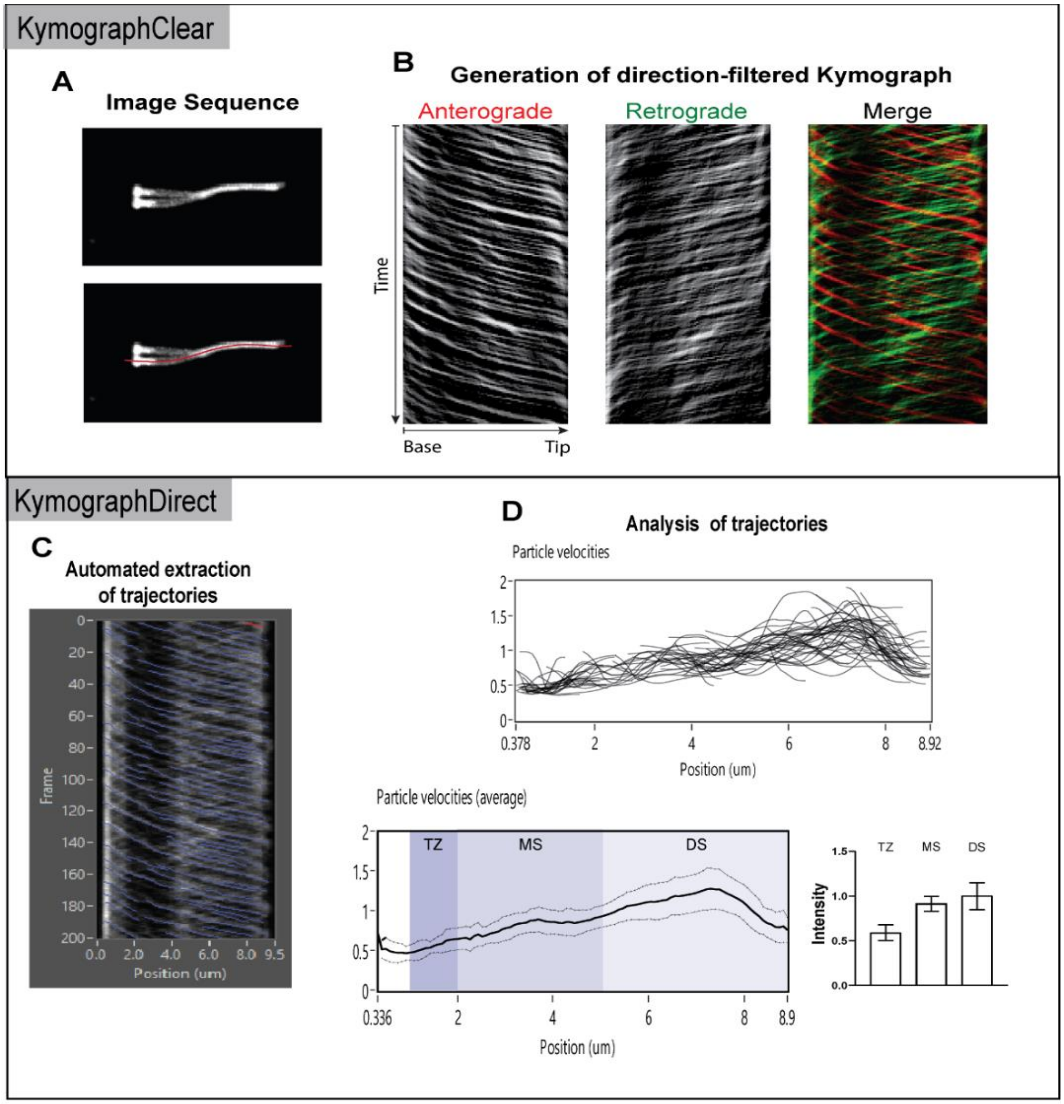

Figure 2.3. Schematic representation of the workflow of image-sequence analysis using KymographClear (A, B) and KymographDirect (C, D). (A) Loading of an image stack and computation of maximum-intensity image of the sequence and generation of the kymograph along a track defined by the user on the maximum-intensity image with subtraction of the background obtained from a user-selected (background) region of interest. The structure observed is a *C. elegans* plasmid cilium. **(B)** Extraction of forward-moving (red) and backward-moving (green) of the kymograph by Fourier filtering. **(C)** Automated detection of trajectories in the background-and bleaching-corrected kymographs (81 blue curves overlaid on the kymograph). **(D)** Results of automated kymograph analysis. Quantitative and statistical analysis of trajectories extracted for position-dependent velocities (top) and average (solid line) and SD (thinner lines) of the position-dependent velocities obtained from all 81 trajectories (bottom), Trajectories were further grouped into three classes (TZ, MS, DS).

Chapter 3 – RESULTS

To dissect the recruitment and ciliary dynamics of dynein-2 subunits, I used GFP/RFP-tagged *C. elegans* strains of dynein-2 HC (CHE-3) and IC (WDR-60), and LIC (XBX-1) that were available in the lab. First, to compare the distribution of WDR-60 and CHE-3 along cilia in *C. elegans,* I crossed both knock-in strains of the IC (WDR-60::GFP) and heavy chain (GFP::CHE-3) with a strain carrying the dynein-2 LIC (XBX-1) fused to a RFP tag in its C-terminus. In both strains, I observed good colocalization between the IC (WDR-60::GFP) or heavy chain (GFP::CHE-3) and the LIC (XBX-1) with similar distributions along cilia **(Figure 3.1)**.

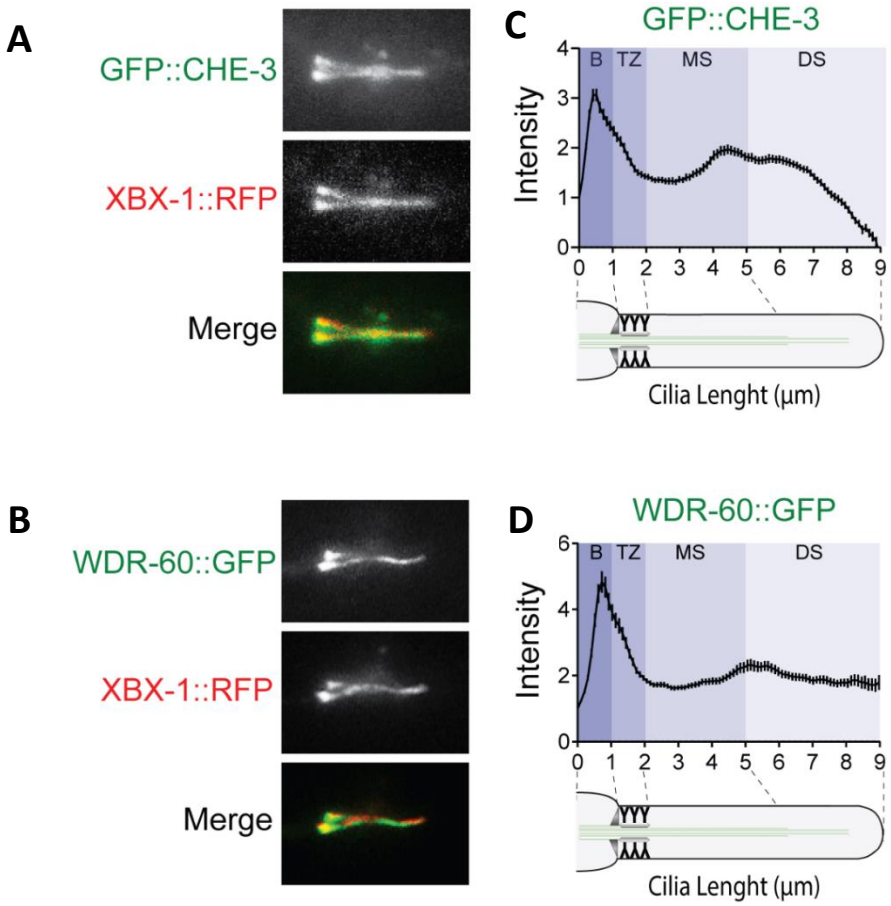

Figure 3.1. GFP::CHE-3 and WDR-60::GFP distribution along cilia. (A-D) WDR-60::3xFLAG::GFP colocalizes with the dynein-2 LIC (XBX-1::RFP::3xFLAG) and its distribution along cilia is similar to the one of the dynein-2 HC (GFP::CHE-3). **(A-B)** Representative phasmid cilia from young adult worms co-expressing GFP::CHE-3 (top) and WDR-60::3xFLAG::GFP (bottom) (green) and XBX-1::RFP::3xFLAG (red). **(C-D)** Quantification of GFP::CHE-3 (top) and WDR-60::3xFLAG::GFP (bottom) signal intensity along cilia; Graphs in **C** and **D** show mean signal intensity ± SEM from at least 80 cilia (~25 worms) and 60 cilia (15 worms), respectively. Schematic of the different cilium subcompartments discriminated in the graph in **C** and **D**. B, cilium Base; TZ, Transition Zone; MS, Middle Segment; DS, Distal Segment (from darker to lighter shades of blue, respectively).

I then analyzed the kinetics of the dynein-2 IC (WDR-60::GFP) or HC (GFP::CHE-3) movement along cilia by performing live imaging and analyzing them using kymographs with

Fourier filtering to discriminate forward-moving, backward-moving and pausing components within each kymograph **(Figure 3.2)**.

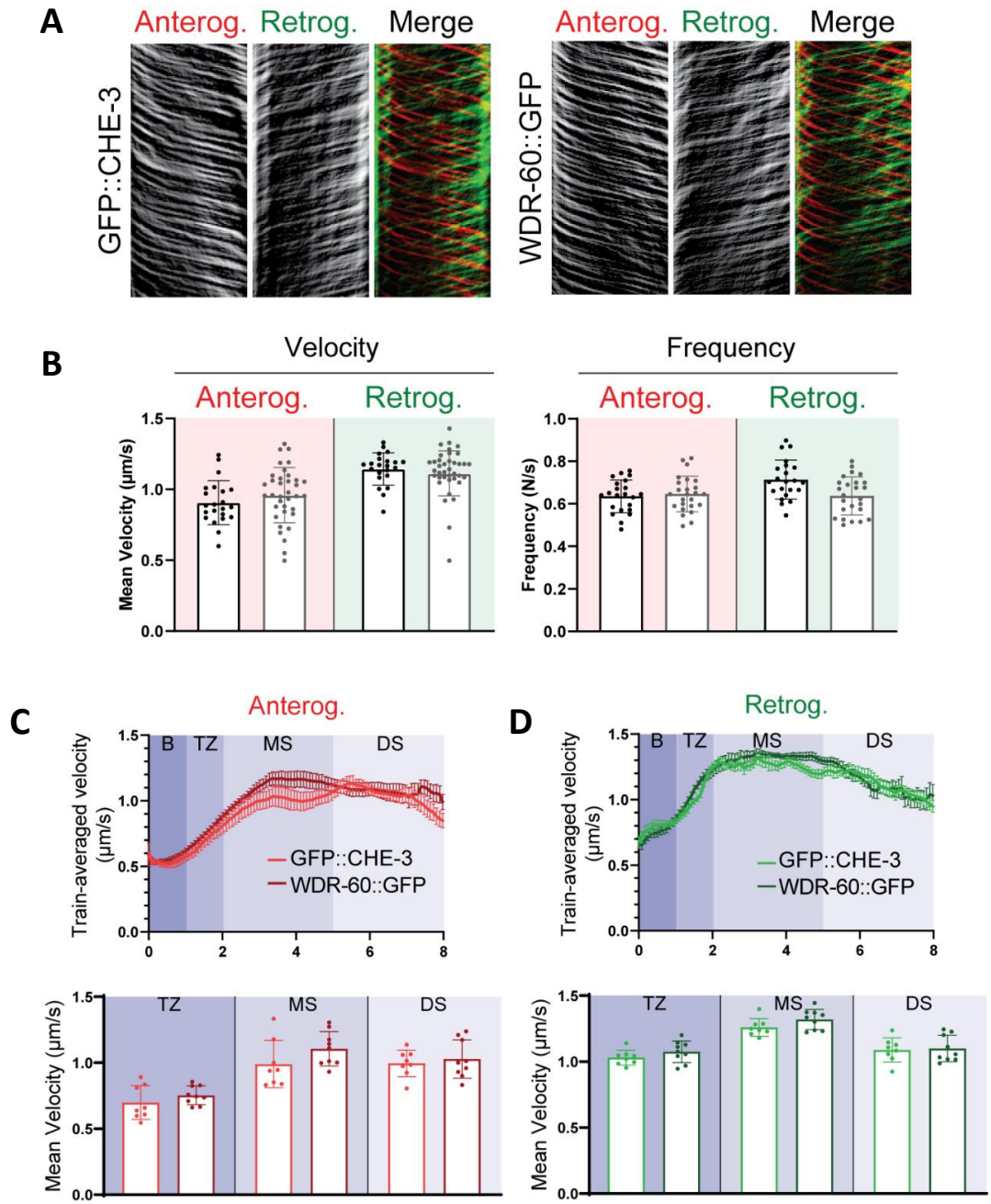

Figure 3.2. Quantifications of average velocity and frequency of both WDR-60::GFP and GFP::CHE-3 in different regions of cilia. (A-D) WDR-60::3xFLAG::GFP IFT kinetics resemble those of GFP::CHE-3. (**A)** Representative kymographs of a phasmid cilium from young adults expressing either GFP::CHE-3 or WDR-60::3xFLAG::GFP, respectively. Single channel for particle moving anterogradely (red) and retrogradely (green), as well as merge channel of both directions, are shown. Vertical scale bars are 5 seconds; horizontal scale bars are 2 µm. (**B)** Mean velocity and frequency of anterograde and retrograde GFP::CHE-3 (light shades) and WDR-60::3xFLAG::GFP (darker shades) particles per kymograph (N>20 worms or 310 particles for the anterograde and 20 particles for the retrograde in a total of at least 3 experiments). Anterograde and retrograde mean velocities per GFP::CHE-3 (light shades) and WDR-60::3xFLAG::GFP (darker shades) particle along cilium are shown in **C** and **D**, respectively, accompanied by the mean velocities for the different cilium subcompartments (N>8 worms or 430 particles in a total of at least 3 experiments). Graphs show average values ± SEM. Scale bars, 2 µm.

These results revealed that the velocity and frequency of the WDR-60::GFP resemble those of the GFP::CHE-3 suggesting that both tagged subunits integrated the ciliary dynein-2 complex and undergo IFT as the human orthologues.

Next, I assayed the behavior of WDR-60 and CHE-3 in WDR-60 and XBX-1 mutants that were made in the lab and received from the BioResource Project of Japan and the CGC *C. elegans* bank. This allowed me to test the interdependence of dynein-2 subunits for their ciliary recruitment.

I started by analyzing by microscopy the distribution of GFP signal in a *wdr-60* null mutant [*wdr-60(tm6453)::GFP*] and in a WDR-60 truncated mutant generated via CRISPR/Cas9-mediated gene editing by my lab colleagues to mimic a Short-Rib Polydactyly Syndrome patient-equivalent mutation that lacks the β-propeller (lacks cDNA encoding 293-673) in the WDR-60 C-terminus [*wdr-60(ΔCT)::GFP*]. I also analyzed the ciliary recruitment/distribution of WDR-60::GFP in an *xbx-1* null mutant. I did not detect any signal in the sensory neurons of *wdr-60(tm6453)::GFP* worms **(Figure 3.3)**, suggesting that no protein is produced in this mutant, in agreement with what a lab colleague observed by western blot. Interestingly, I found that WDR-60(ΔCT)::GFP is still recruited and enters the cilium, although at lower levels, and has a similar distribution along cilium to the WDR-60::GFP control **(Figure 3.3)**, suggesting that the β-propeller domain is not essential for WDR-60 ciliary incorporation.

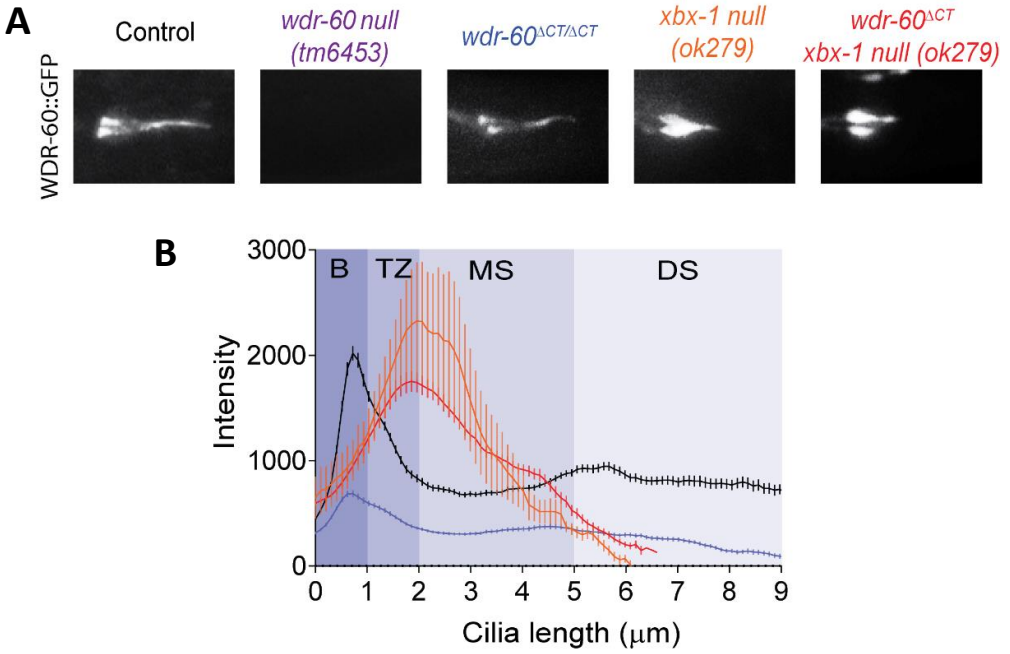

Figure 3.3. Truncation of the WDR-60 β-propeller domain and the loss of the dynein-2 LIC (XBX-1) reduce but do not fully block WDR60 entry into cilia. (A) Representative phasmid cilia for each respective WDR-60 knock-in strain as indicated: the WDR-60 full length with tag knock-in (in black), the null *wdr-60*^{tm6453} with tag knock-in (in purple), the *wdr-60*$^{\Delta CT}$ truncated with tag knock-in (in blue), the WDR-60 full length knock-in in *xbx-1* knock-out (in orange), and the *wdr-60*$^{\Delta CT}$ truncated knock-in in *xbx-1* knock-out (in red). Scale bars, 2 μm. **(B)** Quantification of the mean signal intensity ± SEM of GFP fluorescence signal distribution along the cilium (μm) in the various *wdr-60* mutants labelled in **A**. WDR-60$^{\Delta CT}$::3xFLAG::GFP fluorescence signal, although at lower levels, is still detected in cilium with similar distribution to WDR-60::3xFLAG::GFP. In the absence of XBX-1, both WT and WDR-60$^{\Delta CT}$ accumulate inside the shorter, "stumpy" cilia. Note that no GFP signal is detected in *wdr-*

60^{tm6453}::3xFLAG::GFP strain, validating the full disruption of *wdr-60* in the *tm6453* allele. B, Base of the cilium; TZ, Transition Zone; MS, Middle Segment; DS, Distal Segment (N>17 worms or 40 plasmid cilia in a total of at least 3 experiments).

Previous studies showed that in the absence of the LIC (XBX-1) the heavy chain (CHE-3) cannot be recruited to cilia and, consequently, the ciliary length and structure are affected in *xbx-1* mutants [34, 38]. Using the same *xbx-1* mutant, crossed with WDR-60::GFP, I set up to determine whether loss of the XBX-1 LIC interferes with the ciliary recruitment of the WDR-60 IC. Interestingly, *xbx-1* null mutants expressing either WDR-60::GFP or WDR-60(ΔCT)::GFP still showed GFP signal in cilia of sensory neurons. Both forms of WDR-60 were accumulated at the TZ and in the MS, although the signal of WDR-60(ΔCT)::GFP was slightly decreased when compared with the full length WDR-60::GFP. These results indicated that both WDR-60 and WDR-60(ΔCT) forms can be recruited to cilia independently of the dynein-2 LIC (XBX-1) **(Figure 3.3)**.

We next tested a role for WDR-60 in the recruitment of the dynein-2 HC and LIC to the cilium. For this, we crossed both WDR-60 mutant strains with a strain expressing the heavy chain and the LIC tagged with a N-terminal GFP (GFP::CHE-3) and a C-terminal RFP (XBX-1::RFP), respectively. Interestingly, both GFP::CHE-3 and XBX-1::RFP markers were still detected in cilia from either *wdr-60(tm6453)* or *wdr-60(ΔCT)* mutants by microscopy, indicating that loss of the full-length WDR-60 or of its β-propeller does not prevent the heavy chain (CHE-3) and the LIC (XBX-1) subunits to be recruited to cilia **(Figure 3.4)**. This data suggests that either individual subunits or different sub-complexes of the dynein-2 complex are recruited to cilia before they assemble in a fully functional complex. However, detailed analysis of the GFP::CHE-3 distribution inside the cilium of both WDR-60 mutants revealed that the heavy chain (CHE-3) accumulates near the ciliary base, indicating that dynein-2 IFT is affected in these mutants. Strikingly, cilium length was not altered in the *wdr-60* mutant strains, as the average length of cilium of their sensory neurons is similar to those from the control strain, revealing that although WDR-60 loss alters retrograde IFT, it does not impede cilia formation and axoneme extension in *C. elegans* **(Figure 3.4)**.

Previous studies showed that dynein-2 particles accelerate in the ciliary DS reaching a maximum velocity and then decelerate near to the base [38]. My live imaging and kymograph analysis of GFP::CHE-3 particles in both *wdr-60* mutants showed that anterograde transport was not affected in these worms. However, I observed a strong decrease in the velocity of retrograde transport of GFP::CHE-3 in both WDR-60 mutants.

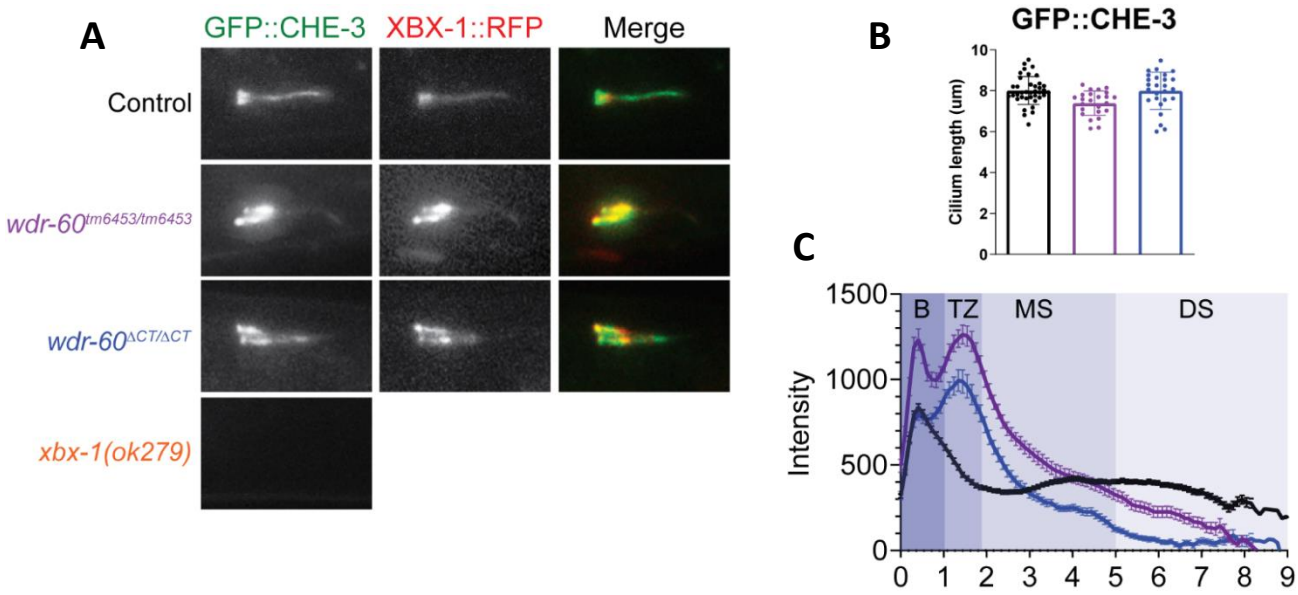

Figure 3.4. Recruitment and distribution of the dynein-2 HC (CHE-3) and LIC (XBX-1) in the absence of the IC (WDR-60). (A-C) GFP::CHE-3 accumulates near the TZ of cilia in phasmid neurons of *wdr-60* mutants. **(A)** Representative phasmid cilia from young adult worms co-expressing GFP::CHE-3 (green) and XBX-1::3xFLAG::RFP (red). **(B)** Average cilia length in the different WDR-60 mutant backgrounds (± SD). **(C)** Average GFP::CHE-3 fluorescence signal intensity along cilia (± SEM). Strains as indicated: control (black), *wdr-60* null (purple), *wdr-60ΔCT* (blue), *xbx-1* null (orange). B, Base of the cilium; TZ, Transition Zone; MS, Middle Segment; DS, Distal Segment (N>~25 worms or 80 plasmid cilia in a total of at least 3 experiments). Scale bars in **A/B**, 2 µm.

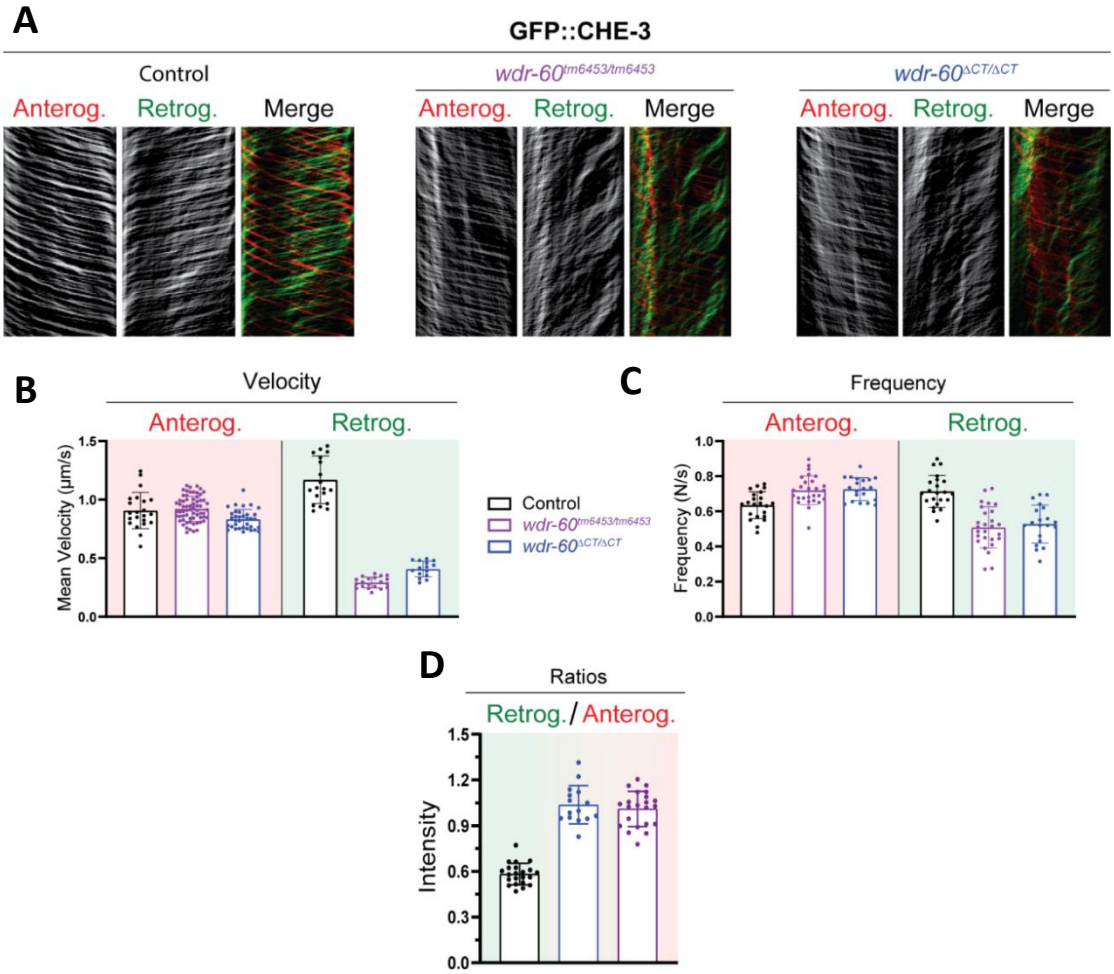

Figure 3.5. Quantifications of average velocity, frequency and ratios of GFP::CHE-3 in WDR-60 mutants. (A-C) Loss of WDR-60 or deletion of its B-propeller significantly reduce GFP-CHE-3 retrograde velocity and frequency. **(A)** Representative kymographs of a phasmid cilia from young adult worms from control (black), *wdr-60* null (purple) and *wdr-60ΔCT* (blue), expressing GFP::CHE-3. Single channel for GFP::CHE-3 particle moving anterogradely (red) and retrogradely (green), as well as merge channel of both directions, are shown. Vertical scale bars are 5 seconds; horizontal scale bars are 2 µm. **(B)** Average velocity and **(C)** frequency of anterograde and retrograde GFP::CHE-3 particles per kymograph. **(D)** Ratio of the intensity of retrograde trains and the intensity of anterograde trains. (N>10 worms or 310 particles for the anterograde and 20 particles for the retrograde in a total of at least 3 experiments). Graphs show average values ± SD.

In fact, I observed that GFP::CHE-3 particles travel at a constant speed along cilia suggesting that mutations in the IC WDR-60 prevent dynein-2 from reaching a maximum velocity **(Figure 3.5)**. Interestingly, my analyses also revealed that the frequency of retrograde movement is decreased in both *wdr-60* mutants. Furthermore, I observed that the ratio between the intensity of retrograde and anterograde trains is increased in *wdr-60* mutants, indicating that retrograde IFT trains contain more dynein-2 particles when WDR-60 is defective **(Figure 3.5)**.

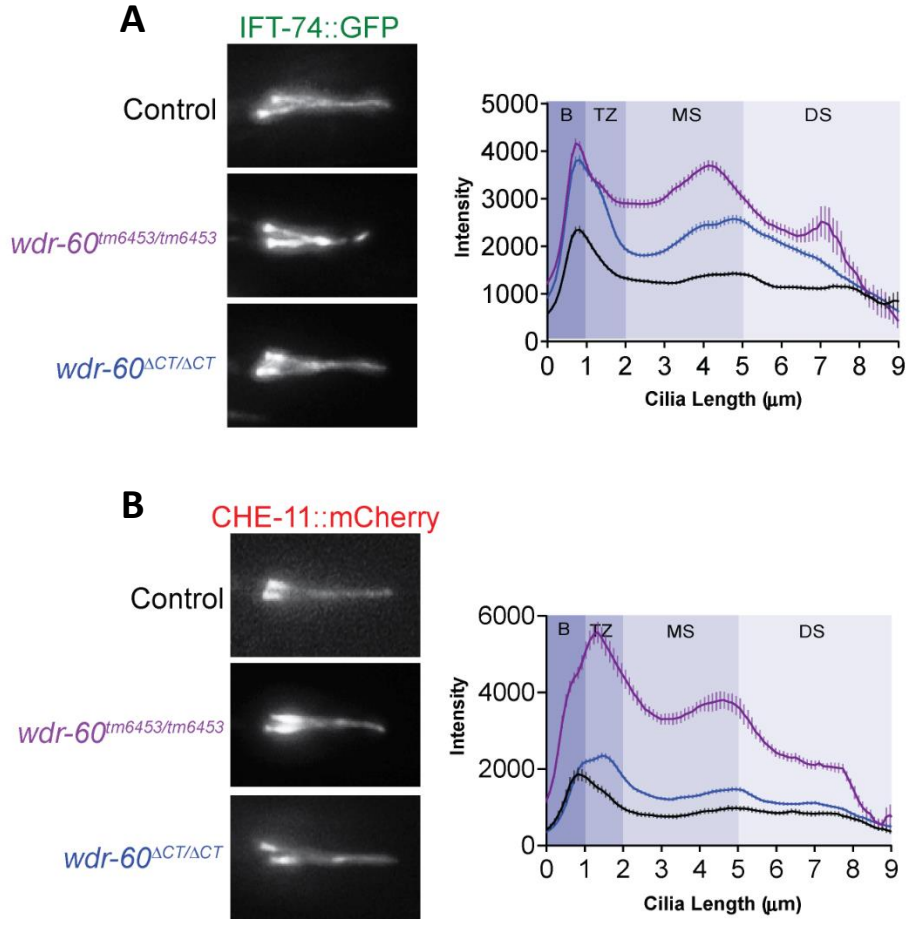

Figure 3.6. IFT-B (IFT-74::GFP) and IFT-A (CHE-11::mCherry) distribution in cilia of WDR-60 mutants. (A) Representative phasmid cilia from young adult worms expressing IFT-74::GFP with its signal intensity along cilia shown in graph (average intensity ± SEM). Strains: control (black), *wdr-60* knock-out (purple) and *wdr-60ΔCT* (blue). B, Base of the cilium; TZ, Transition Zone; MS, Middle Segment; DS, Distal Segment. Scale bars, 2 µm. **(B)** CHE-11::mCherry cilium levels are significantly increased in *wdr-60* mutants, with particles mostly accumulating near the Transition Zone. Representative phasmid cilia from young adult worms expressing CHE-11::mCherry with its signal intensity along cilia shown in graph (average intensity ± SEM). Scale bars, 2 µm.

To test whether WDR-60 loss of function affects other IFT particles, I analyzed the distribution along cilia of fluorophore-tagged proteins that are part of IFT-B (IFT-74::GFP) and

IFT-A (CHE-11/IFT140::mCherry) complexes in both *wdr-60* mutants by microscopy. My analyses of CHE-11::mCherry showed an increase in the signal intensity near the ciliary base, similar to what I observed for GFP::CHE-3, while IFT-74::GFP signal intensity was higher along the full length of the ciliary axoneme in both *wdr-60* mutants **(Figure 3.6)**.

Analyses of kymographs obtained from live imaging revealed that both of these IFT-A and -B markers had unaffected anterograde trains velocity and frequency in both *wdr-60* mutants **(Figure 3.7)**. Interestingly, I found that the retrograde velocity and frequency of both CHE-11::mCherry and IFT-74::GFP were reduced, with an increase in the ratio between the intensity of retrograde and anterograde IFT, similar to what I observed for the heavy chain (CHE-3) **(Figure 3.7)**.

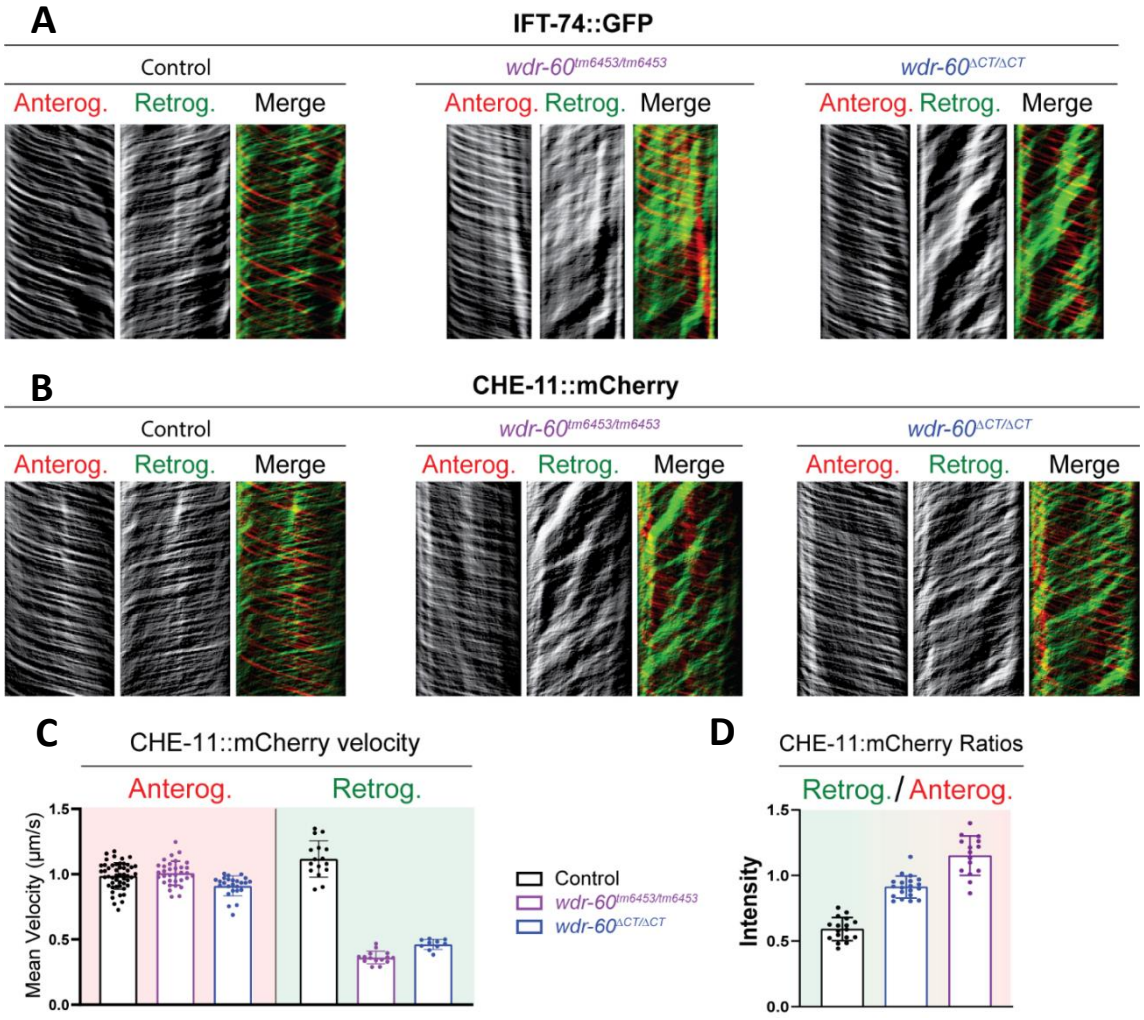

Figure 3.7. IFT-B (IFT-74::GFP) and IFT-A (CHE-11::mCherry) velocity and ratios in WDR-60 mutants. (A,B) IFT-74::GFP and CHE-11::mCherry have reduced retrograde velocity and frequency in *wdr-60* mutants. Representative kymographs of a phasmid cilia from young adult worms from the indicated strains expressing either **(A)** IFT-74-GFP or **(B)** CHE-11::mCherry. Single channels for particle moving anterogradely (red) and retrogradely (green), as well as merge channels of both directions, are shown. Vertical scale bars are 5 seconds; horizontal scale bars are 2 µm. **(C,D)** Mean velocity and intensity of anterograde and retrograde CHE-11::mCherry particles (N>10 worms or 540 particles for the anterograde and 20 particles for the retrograde in a total of at least 3 experiments). Graphs show average values ± SD.

I further tested if both kinesin-2 (KAP-1::GFP, a kinesin-2 binding component) and OSM-3 (OSM-3::mCherry) could be affected in the absence of the IC WDR-60. I found that kinesin-2 distribution has accumulations near the ciliary base similar to what I found for GFP::CHE-3 and CHE-11::mCherry **(Figure 3.8)**, while OSM-3 had a similar distribution to the control with a slight increase of signal along cilia. Together my data supports an essential role of WDR-60 for dynein-2 activity and retrograde IFT in *C. elegans* **(Figure 3.8)**.

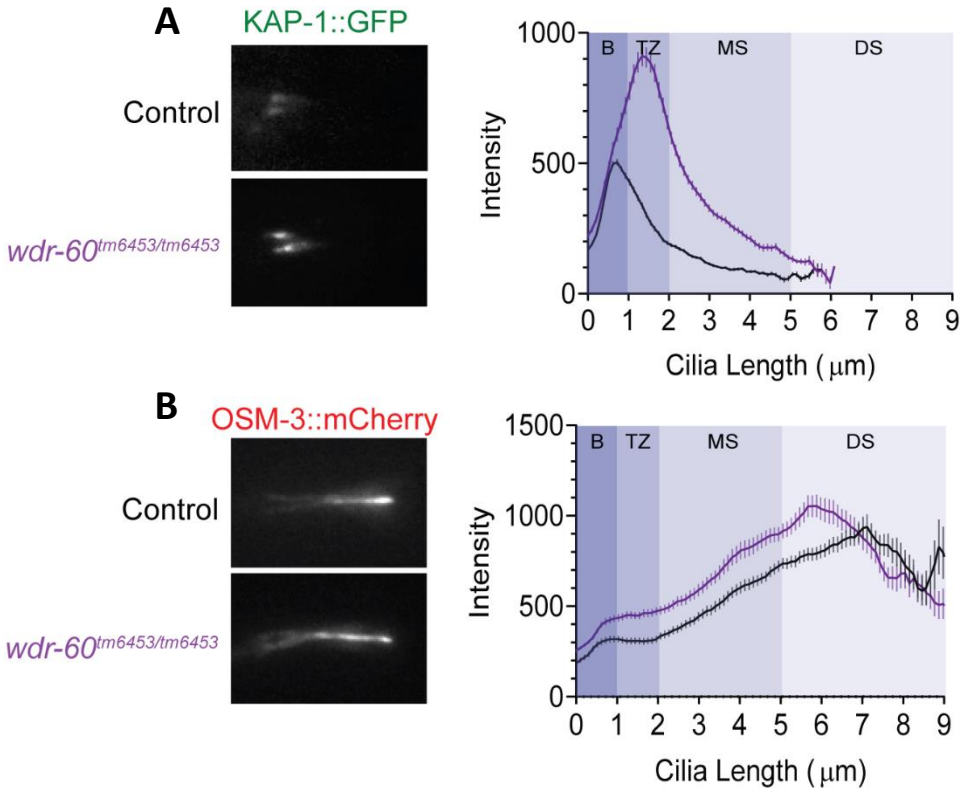

Figure 3.8. KAP-1::GFP (kinesin-2) and OSM-3::mCherry (osm-3) localization and distribution in *wdr-60* mutants. (A) KAP-1::GFP cilium levels are significantly increased in *wdr-60* mutants, with particles mostly accumulating near the Transition Zone. Representative phasmid cilia from young adult worms expressing KAP-1::GFP with its signal intensity along cilia shown in graph (average intensity ± SEM). Strains: control (black) and *wdr-60* knock-out (purple). B, Base of the cilium; TZ, Transition Zone; MS, Middle Segment; DS, Distal Segment. Scale bars, 2 µm. **(B)** Representative phasmid cilia from young adult worms expressing OSM-3::mCherry with its signal intensity along cilia shown in graph (average intensity ± SEM). Scale bars, 2 µm.

To understand if the effects of the WDR-60 mutations on IFT could affect the worm behavior, I analyzed cilia-dependent behavior in the two *wdr-60* mutants **(Figure 3.9)**. I assayed mating efficiency which is known to rely on sensory signals given by the hermaphrodite that are sensed by the cilia of the male tail for mating [53]. The read out in the mating assay is the presence of male worms in the F1 progeny in a number superior to that expected from random mis-segregation of the X-chromosome seen from hermaphrodite self-fertilization (~2%). Male worms with cilia defects cannot sense the signal excreted by the hermaphrodite and, therefore, do not mate, giving rise mostly to hermaphrodites in the F1 progeny (with the exception of ~2% of males that occur due to random mis-segregation of the

X chromosome). To generate males of all the strains to be tested, I initially crossed hermaphrodites of these strains with males carrying a mutation in the *him-8* gene which is known to affect crossing-over between the X homolog chromosomes during meiosis and lead to their mis-segregation. As a result, *him-8* strains tend to give rise to ~50% males in their progeny. To exclude the possibility that *him-8* mutants could have any effect in the mating efficiency of our *wdr-60* mutants, I included the *him-8* single mutant strain in the mating assay **(Figure 3.9)**.

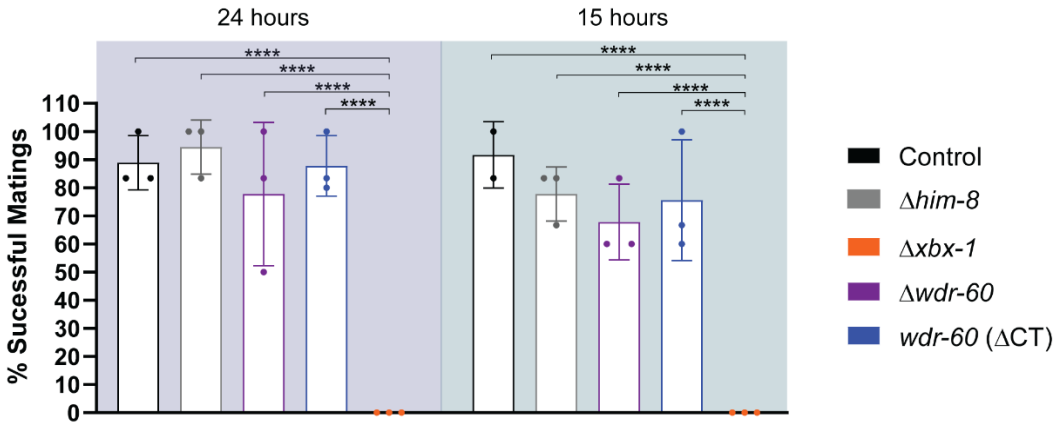

Figure 3.9. Mating assay to test the efficiency of sensory cilia functions in *wdr-60* mutants. Mating success – score of 0% (no mating) or 100% (mating) for each hermaphrodite singled out. Strains as indicated: the WDR-60 full length (in black), the WDR-60 full length in *him-8* knock-out (in gray) the *xbx-1* knock-out in *him-8* knock-out (in orange), the null *wdr-60(tm6453)* in *him-8* knock-out (in purple) and the *wdr-60ΔCT* truncated *him-8* knock-out (in blue). Blue Square – Mating occurred for 24 hours. Green Square – Mating occurred for 15 hours.

I also performed an osmotic assay that tested the tolerance of worms to high osmolarity, which is sensed by their sensory cilia. This assay consists in placing worms inside a ring of a highly concentrated glycerol solution on a plate. In contact with the ring, wild-type worms turn around while worms that have cilia defects fail to sense high osmolarity and escape the ring being categorized as “Escapers”. In both assays, I used worms N2 as a positive control for sensory cilia functions, and worms Δ*xbx-1* as a negative control due to their incapability to form a normal size cilium and therefore to sense their environment **(Figure 3.10)**.

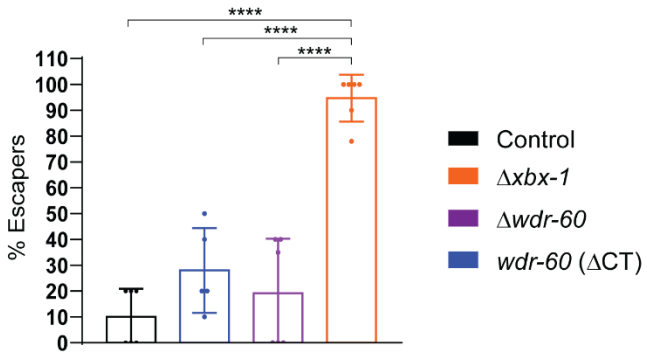

Figure 3.10. Osmotic avoidance assay to test the efficiency of sensory cilia functions in *wdr-60* mutants. Osmotic Avoidance assay to test whether sensory cilia *wdr-60* mutant strains can detect hypertonic glycerol barrier

and respond by reversing backwards (graph shows mean fraction of worms (± SD, N=5 worms in a total of at least 4 experiments) that fail to sense the high glycerol concentrations of the ring surrounding them, and cross it to escape). Strains as indicated: the WDR-60 full length (in black), the WDR-60 full length in *him-8* knock-out (in gray) the *xbx-1* knock-out in *him-8* knock-out (in orange), the null *wdr-60*(tm6453) in *him-8* knock-out (in purple) and the *wdr*-60ΔCT truncated *him-8* knock-out (in blue).

My results from both assays showed that the two *wdr-60* mutant strains have small but significant defects in mating efficiency and osmotic tolerance when compared to the N2 control **(Figure 3.9 and 3.10)**. However, the behavioral defects of *wdr-60* mutants are mild when compared to *xbx-1* null strain, suggesting that although WDR-60 is important for IFT proficiency, their cilia are at least partially functional for the sensory functions tested.

Previous studies showed that dynein-2 HC is essential to maintain the integrity of the ciliary TZ and for retrograde trafficking of IFT particles [7, 41]. Given that dynein-2 HC (CHE-3) and other IFT particles accumulate near the base of cilia in *wdr-60* mutants, we wondered if this could be due to problems in the TZ **(Figure 3.11)**. To test this hypothesis, I analyzed the distribution of two distinct TZ markers in *wdr-60* and *xbx-1* mutants: TMEM-107::GFP and MKS-6::mCherry, both present in the MKS module. While the distribution of both markers in the *wdr-60* mutants was confined to the TZ as in control, these markers were mislocalized and extended along cilia in the *xbx-1* mutant similar to that published for *che-3*. These results suggested that loss of the IC WDR-60 did not disrupt the organization of the ciliary TZ **(Figure 3.11)**.

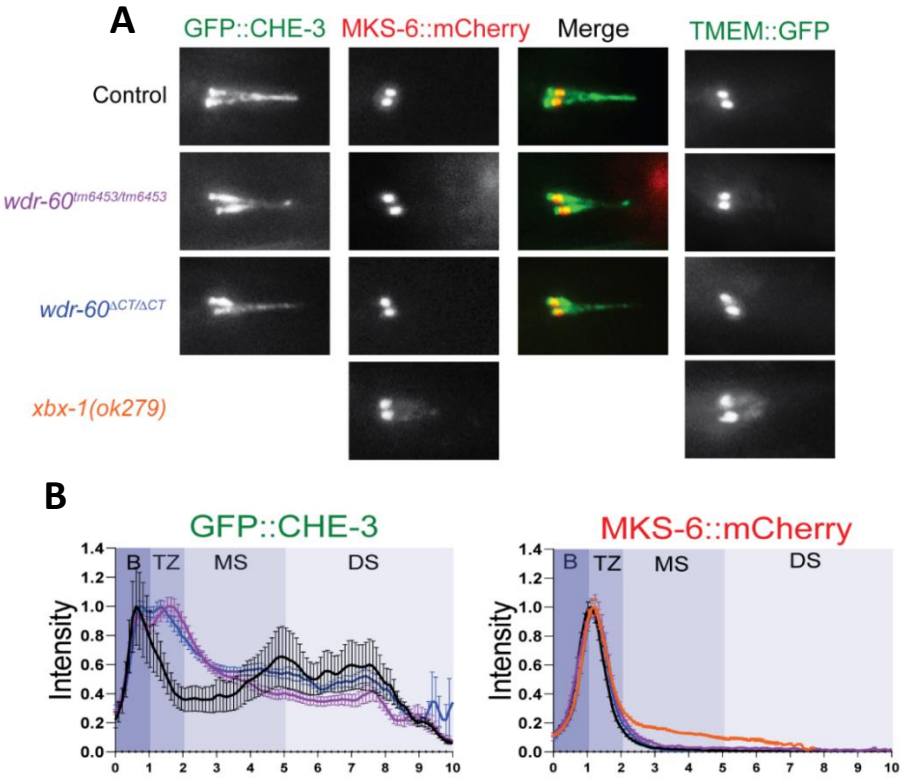

Figure 3.11. Localization of the dynein-2 Heavy Chain (GFP::CHE-3) relative to Transition Zone components (MKS-6::mCherry and TMEM::GFP) in the absence of specific dynein-2 subunits. (A) Representative phasmid cilia from young adult worms co-expressing GFP::CHE-3 (green) and MKS-6::mCherry (red). Representative phasmid cilia from young adult worms expressing TMEM::GFP. As seen for MKS-6::mCherry, the TMEM::GFP fluorescence signal is confined to the Transition Zone in both WT and *wdr-60* mutants, which contrasts to the more dispersed TMEM::GFP signal observed in *xbx-1* knock-out worms. **(B)** Quantification of the GFP::CHE-3 and MKS-6::mCherry signal intensities along cilia shown in (average intensity ± SEM, N>14 worms or 35 plasmid cilia in a total of at least 3 experiments).

Interestingly, colocalization of GFP::CHE-3 with MKS-6::mCherry showed that CHE-3 accumulation in cilia of *wdr-60* mutants was localized just next to the distal side of the TZ, suggesting that dynein-2 HC might have difficulty in crossing the TZ and exiting the cilium **(Figure 3.12)**.

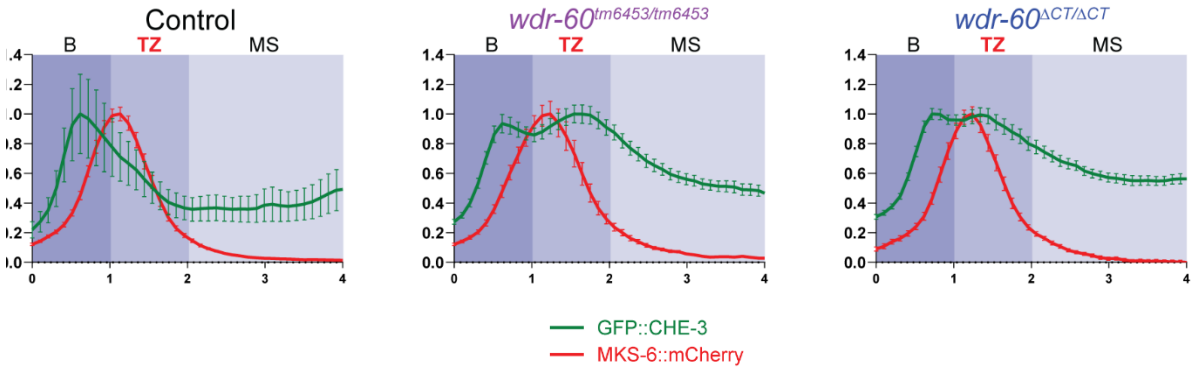

Figure 3.12. Localization of dynein-2 Heavy Chain (GFP::CHE-3) relative to a Transition Zone component (MKS-6::mCherry) in *wdr-60* mutants. Zoomed-in representation of the data in **Figure X (B)** to better visualize the overlap of the dynein-2 HC signal with the TZ marker. In contrast to *xbx-1* knock-out worms, which show a more dispersed MKS-6::mCherry signal along cilium, the MKS-6::mCherry signal is well confined to the Transition Zone in *wdr-60* mutants as in WT controls. The GFP::CHE-3 accumulations observed inside the cilia of *wdr-60* mutants occur immediately before crossing the TZ (on the inner side). Strains: control (black), *wdr-60* knock-out (purple), *wdr-60ΔCT* (blue), and *xbx-1* null (orange). B, Base of the cilium; TZ, Transition Zone; MS, Middle Segment; DS, Distal Segment. Scale bars, 2 µm.

These results led us then to hypothesize that if the barrier/TZ could be removed this might allow the exit of dynein-2 HC and IFT particles from cilia, thus, rescuing the IFT accumulations seen in *wdr-60* mutants. In this context, we found an interesting study showing that loss of key components from the MKS and NPHP complexes block the assembly of the TZ Y-links resulting in detachment and dilation of the ciliary membrane, while leaving the central cylinder and associated axonemal microtubules intact [14]. Therefore, to test our hypothesis, we used a single KO mutant for MKSR-2 and a double mutant for the same protein and NPHP-4 to disrupt the assembly of Y-links in the *wdr-60*(tm6453) mutant **(Figure 3.13)**. strikingly, our results showed that complete disruption of the Y-links, by loss of both components of the MKS and NPH complexes, resulted in the rescue of GFP::CHE-3 accumulations that I had observed in the absence of WDR-60, perhaps by facilitating the exit of dynein-2 and other components from cilia **(Figure 3.13)**.

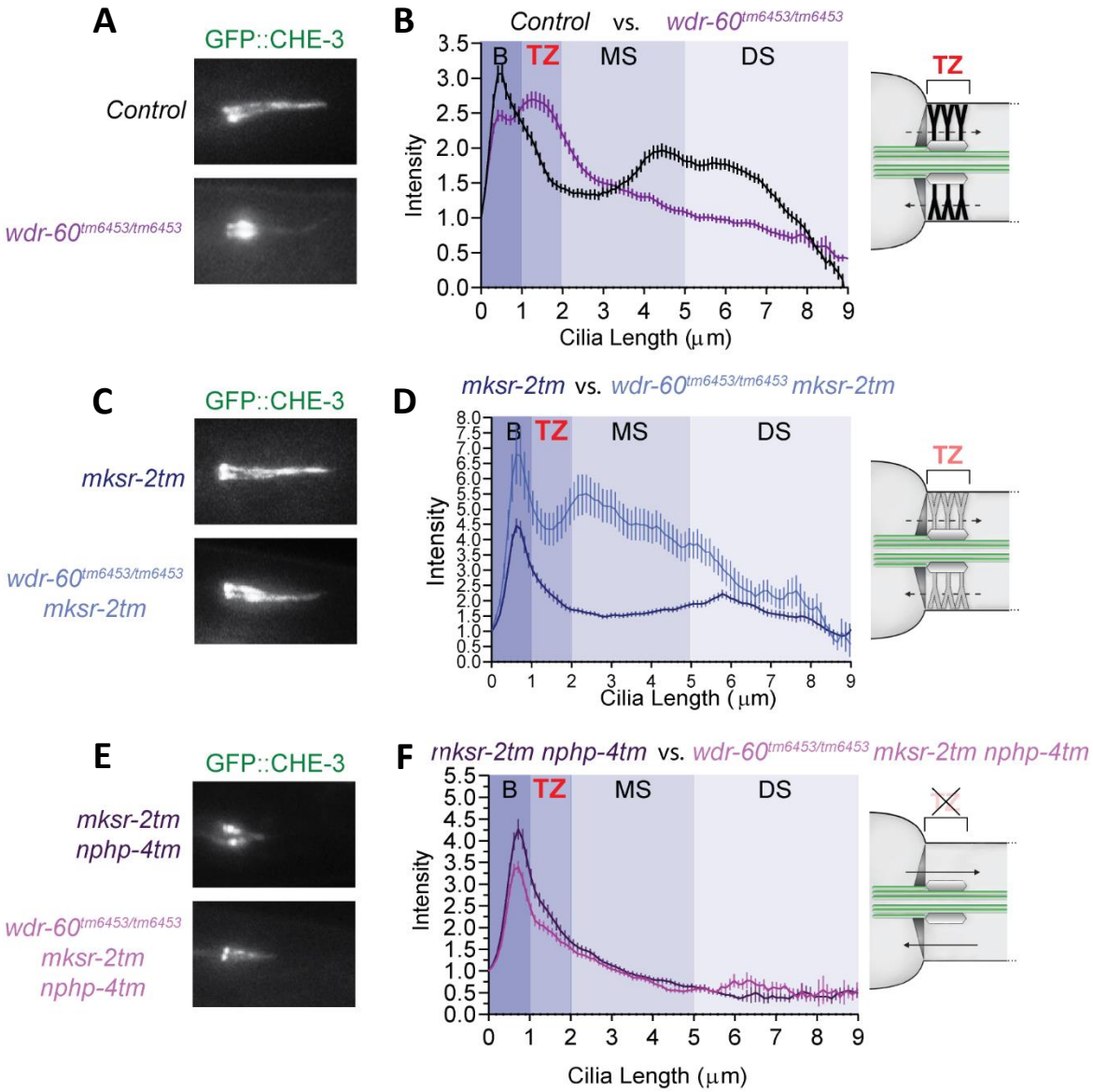

Figure 3.13. GFP::CHE-3 distribution inside cilia of *wdr-60* mutants upon the disruption of the Transition Zone Y-links. (A) Representative phasmid cilia from young adult worms expressing GFP::CHE-3. **(B)** Graph with the average signal intensity along cilia (normalized to the base, ± SEM, N>25 worms or 80 plasmid cilia in a total of at least 3 experiments) in control (black) and *wdr-60* knock-out (purple) worms. Schematic drawing of a wild-type cilium base and with Transition Zone. In WDR-60-deficient cilia, CHE-3::GFP is unable to cross the Transition Zone and exit cilia. **(C,E)** Representative examples of phasmid cilia from young adult worms of the labelled genotypes, expressing GFP::CHE-3. **(D,F)** Graphs with the average signal intensity along cilia (normalized to the base, ± SEM, N>12 worms or 30 plasmid cilia in a total of at least 3 experiments) for each of the indicated mutants. Schematic drawings of cilia in mutants as indicated. Complete disruption of the Y-links, by co-disrupting two central components of the MKS and NPH modules, rescued the GFP::CHE-3 accumulation previously observed in the absence of WDR-60, facilitating dynein-2 exit from cilia. Strains: *mksr-2tm* (dark blue), *wdr-60* knock-out *mksr-2tm* (light blue), *mksr-2tm nphp-4tm* (dark purple), and *wdr-60* knock-out *mksr-2tm nphp-4tm* (pink). B, Base of the cilium; TZ, Transition Zone; MS, Middle Segment; DS, Distal Segment. Scale bars, 2 µm.

Chapter 4 – DISCUSSION

In this study, I dissected the relative importance of dynein-2 IC (WDR-60) and LIC (XBX-1) for the mechanisms behind the recruitment of dynein-2 HC (CHE-3) to cilia and their contribution to retrograde IFT and worm behavior.

Dynein-2 is composed of two copies of dynein-2 HC that present a combination of symmetrical and asymmetrical regions in their conformation. While their motor domain adopts a symmetrical conformation, their N-terminal tails are asymmetrical such that one HC steers into a straight conformation whereas the second into a zig-zag conformation [37]. The different conformations of the two HCs are thought to be important for dynein-2 incorporation into IFT trains and to result in part from the binding of the heterodimer of ICs composed of WDR60 and WDR34, which hold the two copies of dynein-2 HC tails of the Dynein-2 complex in the proper position. It is known that the bond between dynein-2 HC and the ICs is accomplished by the β-propeller of both ICs (WDR60 and WDR34), while their N-termini promote their dimerization through the LCs [37].

It has also been reported that loss of some components of dynein-2 modifies the stability of the whole dynein-2 complex. For example, in human cells, in *C. elegans* and in *Chlamydomonas*, absence of the LIC destabilizes the HC [38, 54, 55]. The importance of other dynein-2 subunits for the complex stability and functions is still unclear. During this project, I compared the loss of the LIC with the IC to determine whether the loss of the latter (WDR-60) could destabilize the dynein-2 complex, presumably by disrupting the asymmetry of the two dynein-2 HC and, consequently, affect IFT and ciliogenesis.

For this, we took advantage of a clean genetic system in *C. elegans* to study the impact of the loss of function of the WDR-60 IC and the XBX-1 LIC in dynein-2 ciliary recruitment, kinetics and cilia structure in sensory neurons. In addition to using a knock-out strains, I took advantage of a truncated version of WDR-60 lacking the β-propeller domain that mimics a mutation found in a SRPS patient, that was made by a colleague in the lab. By analyzing the recruitment of different dynein-2 subunits using GFP/RFP-tagged knock-in strains, my data showed that while loss of the dynein-2 LIC (XBX-1) prevented the HC (GFP::CHE-3) to be recruited to cilia as expected, it did not affect the recruitment of the IC (WDR-60). Interestingly, absence of WDR-60 did not prevent the recruitment of either LIC or HC. These findings further demonstrate that the recruitment of both dynein-2 HC and LIC to cilia is dependent on each other and reveals that it can still occur independently of the IC WDR-60. It is also possible that other IC is present in *C. elegans* as in human cells (WDR34), and that this subunit might be sufficient to stabilize the dynein-2 complex in the absence of WDR-60. To date there is no clear ortholog of WDR34 identified in *C. elegans*. That being said, using sequence analyses, my colleagues in the lab have found that the *C. elegans* dynein-1 IC DYCI-1 is the closest related to human WDR34, and thus, it is conservable that it also functions in the ciliary dynein-2

complex. In agreement with this hypothesis, DYCI-1 has been previously detected in cilia of *C. elegans* sensory neurons [56]. In this context, it would be interesting to look at DYCI-1 in our *wdr-60* mutants in future experiments.

Interestingly, I also observed that the loss of the β-propeller of WDR-60 did not prevent WDR-60(ΔCT) recruitment to base of the cilia, neither other dynein-2 subunits (HC and LIC) incorporation into the IFT trains. Thus, my data reveals that the N-terminus of WDR-60 might still be capable of binding to the LCs, and possibly to another IC such as DYCI-1; however, this needs further investigation. Nevertheless, lower levels in the signal of WDR-60 were observed in the cilia in the absence of the WDR-60 β-propeller revealing some role for this domain in its ciliary recruitment. Even though the recruitment of GFP::CHE-3 and XBX-1::RFP in the *wdr-60* mutants was not affected, my colleagues and I observed some defects in the retrograde IFT kinetics.

By using kymographs with Fourier filtering, I analyzed the velocity and frequency of different IFT markers in our *wdr-60* mutants, including dynein-2 subunits. Through this I was able to show that loss or truncation of the WDR-60 IC did not affect anterograde transport of dynein-2 HC and IFT components, consistent with WDR-60 being dispensable for the activity of kinesins and the incorporation of dynein-2 into the IFT trains. However, I also found that WDR-60 loss of function prevents dynein-2 from reaching the maximum velocity in the retrograde direction, travelling with constant speed along cilia, with less IFT trains but more motor particles per train. These data demonstrate an important role for WDR-60 in dynein-2 activity and ciliary retrograde transport.

A recent study found that the *C. elegans* dynein-2 HC (CHE-3) is required for the correct TZ assembly and gating function [32]. Here I found that, in addition to the HC, the LIC (XBX-1) is also important for the maintenance of the ciliary TZ in *C. elegans*, as different TZ markers (MKS-6::mCherry and TMEM-107::GFP) are mislocalized inside cilia in the absence of XBX-1. Interestingly, loss of the WDR-60 IC did not affect the organization of the ciliary TZ, although subunits of the dynein-2 complex and IFT particles were accumulating inside cilia near the ciliary base (more specifically in the distal part of the TZ). In agreement, a previous study found that WDR60 KO in hTERT-RPE-1 cells also leads to accumulations of IFT particles inside cilia, similar to my results [41]. However, in contrast to our observations in *C elegans*, they also reported disruptions in the organization of the ciliary TZ in WDR60 KO cells. It is conceivable that in human cells loss of WDR60 leads to destabilization of the dynein-2 complex, which would indirectly affect the TZ structure, however this possibility was not addressed in the referred study.

Williams, C.L. *et al.* [14] found that the disrupting of two TZ modules (MKS/MKSR and NPHP) lead to the abolition of Y-links in the TZ. In the present study, I found that by mutating both components of the MKS and NPH complexes, and presumably disrupting the TZ Y-links, the GFP::CHE-3 accumulations observed upon the loss of WDR-60 were rescued. These findings suggest that WDR-60 regulates the passage of the dynein-2 complex and IFT particles through the TZ to allow their ciliary exit, supporting an interplay between components of the TZ and particles from retrograde transport. Altogether, my results demonstrate important roles for WDR-60 at multiple stages of IFT: in dynein-2 activity, ciliary retrograde transport and exit of IFT components from cilia. We envision several non-mutually exclusive scenarios that might explain my results: i) WDR-60-deficient dynein-2 is unable to reach the velocity/force necessary to pass the dense TZ region; ii) WDR-60-deficient dynein-2 cannot interact with the TZ to allow the exit of retrograde IFT motors from cilia; iii) without WDR-60, the dynein-2 HC (CHE-3) are misaligned and, consequently, the defective dynein-2 complex is unable to cross the dense protein region at the TZ. Further experiments are necessary to dissect these hypotheses and the functional interactions between the dynein-2 subunits and the TZ.

A recent imaging study on *Chlamydomonas* flagella revealed that IFT-B proteins from retrograde IFT trains can be reused in anterograde trains [57]. Similarly, in *C. elegans*, recent evidence suggests that motor proteins returning from cilia turn around and re-enter the cilium [58, 59]. In the present study, I observed that markers of IFT-A (CHE-11::mCherry) and IFT-B (IFT-74::GFP) had defects in the distribution along cilia, similar to those observed for the dynein-2 HC and LIC, with an increase in the overall signal in cilia. The incapability of IFT trains to pass through the TZ, and consequently, exit cilia in the *wdr-60* mutants could prevent the recycling of IFT components at the ciliary base, explaining these accumulations inside the cilium. Of note, single molecule studies showed that dissociated kinesin-2 motors also undergo rapid turnaround and recycling at the ciliary base, whereas OSM-3 is recycled mainly near the MS [59]. Interestingly, when combining markers of both kinesins (KAP-1::GFP and OSM-3::mCherry) with our *wdr-60* mutations, I observed that while the distribution of kinesin-II (KAP-1::GFP) had similar defects to what was observed for the HC and LIC, I did not observe accumulations of OSM-3::mCherry, suggesting that WDR-60 loss of function leads to a defect in the recycling of IFT components at the ciliary base. Thus, my data is in agreement with a closed model in cilia where IFT components are recycled at the ciliary base, and this is disrupted in the *wdr-60* mutants possibly due to defects in the passage of IFT components through the TZ that impede their ciliary exit, and consequently, their recycling.

Remarkably, even though WDR-60 loss of function leads to a combination of defects in dynein-2 activity, retrograde transport of IFT particles, frequency and size of retrograde IFT trains, ciliary exit of IFT trains, and recycling of IFT particles, my data further showed the cilia

length in both *wdr-60* mutants was not affected and thus WDR-60 is dispensable for completing cilia assembly, which agrees with published studies in hTERT-RPE1 cells [41]. Strikingly, my behavior assays in the *wdr-60* mutants showed that, in the absence of WDR-60, cilia were still partially functional for the sensory functions tested, with only a slight decrease in the efficiency of mating or osmotic sensing. It is possible that other cilia-dependent signaling pathways might be more affected in our *wdr-60* mutants. It is also possible that WDR-60 functions affect the structure and sensory functions of specific subtypes of cilia. Here I analyzed amphid, phasmid and AWC cilia, but *C. elegans* possess a total of 60 cilia with distinct morphologies at dendritic endings of sensory neurons. Therefore, other cilia types and behavioral tests need to be performed in our *wdr-60* mutants to further explore these possibilities.

Chapter 5 – BIBLIOGRAPHY

1. Singla, V. and J.F. Reiter, *The primary cilium as the cell's antenna: signaling at a sensory organelle.* Science, 2006. **313**(5787): p. 629-33.
2. Choksi, S.P., et al., *Switching on cilia: transcriptional networks regulating ciliogenesis.* Development, 2014. **141**(7): p. 1427-41.
3. Green, J.A. and K. Mykytyn, *Neuronal ciliary signaling in homeostasis and disease.* Cell Mol Life Sci, 2010. **67**(19): p. 3287-97.
4. Louvi, A. and E.A. Grove, *Cilia in the CNS: the quiet organelle claims center stage.* Neuron, 2011. **69**(6): p. 1046-60.
5. Waters, A.M. and P.L. Beales, *Ciliopathies: an expanding disease spectrum.* Pediatr Nephrol, 2011. **26**(7): p. 1039-56.
6. Hildebrandt, F., T. Benzing, and N. Katsanis, *Ciliopathies.* N Engl J Med, 2011. **364**(16): p. 1533-43.
7. Garcia-Gonzalo, F.R. and J.F. Reiter, *Open Sesame: How Transition Fibers and the Transition Zone Control Ciliary Composition.* Cold Spring Harb Perspect Biol, 2017. **9**(2).
8. Nachury, M.V., *The molecular machines that traffic signaling receptors into and out of cilia.* Curr Opin Cell Biol, 2018. **51**: p. 124-131.
9. Chih, B., et al., *A ciliopathy complex at the transition zone protects the cilia as a privileged membrane domain.* Nat Cell Biol, 2011. **14**(1): p. 61-72.
10. Dowdle, W.E., et al., *Disruption of a ciliary B9 protein complex causes Meckel syndrome.* Am J Hum Genet, 2011. **89**(1): p. 94-110.
11. Garcia-Gonzalo, F.R., et al., *A transition zone complex regulates mammalian ciliogenesis and ciliary membrane composition.* Nat Genet, 2011. **43**(8): p. 776-84.
12. Roberson, E.C., et al., *TMEM231, mutated in orofaciodigital and Meckel syndromes, organizes the ciliary transition zone.* J Cell Biol, 2015. **209**(1): p. 129-42.
13. Sang, L., et al., *Mapping the NPHP-JBTS-MKS protein network reveals ciliopathy disease genes and pathways.* Cell, 2011. **145**(4): p. 513-28.
14. Williams, C.L., et al., *MKS and NPHP modules cooperate to establish basal body/transition zone membrane associations and ciliary gate function during ciliogenesis.* J Cell Biol, 2011. **192**(6): p. 1023-41.
15. Reiter, J.F., O.E. Blacque, and M.R. Leroux, *The base of the cilium: roles for transition fibres and the transition zone in ciliary formation, maintenance and compartmentalization.* EMBO Rep, 2012. **13**(7): p. 608-18.
16. Schouteden, C., et al., *The ciliary transition zone functions in cell adhesion but is dispensable for axoneme assembly in C. elegans.* J Cell Biol, 2015. **210**(1): p. 35-44.
17. Ward, S., et al., *Electron microscopical reconstruction of the anterior sensory anatomy of the nematode Caenorhabditis elegans.?2UU.* J Comp Neurol, 1975. **160**(3): p. 313-37.
18. Perkins, L.A., et al., *Mutant sensory cilia in the nematode Caenorhabditis elegans.* Dev Biol, 1986. **117**(2): p. 456-87.
19. Prevo, B., J.M. Scholey, and E.J.G. Peterman, *Intraflagellar transport: mechanisms of motor action, cooperation, and cargo delivery.* FEBS J, 2017. **284**(18): p. 2905-2931.
20. Rosenbaum, J.L. and G.B. Witman, *Intraflagellar transport.* Nat Rev Mol Cell Biol, 2002. **3**(11): p. 813-25.
21. Scholey, J.M., *Intraflagellar transport.* Annu Rev Cell Dev Biol, 2003. **19**: p. 423-43.
22. Kozminski, K.G., P.L. Beech, and J.L. Rosenbaum, *The Chlamydomonas kinesin-like protein FLA10 is involved in motility associated with the flagellar membrane.* J Cell Biol, 1995. **131**(6 Pt 1): p. 1517-27.
23. Chien, A., et al., *Dynamics of the IFT machinery at the ciliary tip.* Elife, 2017. **6**.
24. Buisson, J., et al., *Intraflagellar transport proteins cycle between the flagellum and its base.* J Cell Sci, 2013. **126**(Pt 1): p. 327-38.
25. Iomini, C., et al., *Protein particles in Chlamydomonas flagella undergo a transport cycle consisting of four phases.* J Cell Biol, 2001. **153**(1): p. 13-24.

26. Wren, K.N., et al., *A differential cargo-loading model of ciliary length regulation by IFT.* Curr Biol, 2013. **23**(24): p. 2463-71.
27. Bhogaraju, S., et al., *Getting tubulin to the tip of the cilium: one IFT train, many different tubulin cargo-binding sites?* Bioessays, 2014. **36**(5): p. 463-7.
28. He, M., S. Agbu, and K.V. Anderson, *Microtubule Motors Drive Hedgehog Signaling in Primary Cilia.* Trends Cell Biol, 2017. **27**(2): p. 110-125.
29. Ishikawa, H. and W.F. Marshall, *Ciliogenesis: building the cell's antenna.* Nat Rev Mol Cell Biol, 2011. **12**(4): p. 222-34.
30. Sung, C.H. and M.R. Leroux, *The roles of evolutionarily conserved functional modules in cilia-related trafficking.* Nat Cell Biol, 2013. **15**(12): p. 1387-97.
31. Orozco, J.T., et al., *Movement of motor and cargo along cilia.* Nature, 1999. **398**(6729): p. 674.
32. Jensen, V.L., et al., *Role for intraflagellar transport in building a functional transition zone.* EMBO Rep, 2018. **19**(12).
33. Nakayama, K. and Y. Katoh, *Architecture of the IFT ciliary trafficking machinery and interplay between its components.* Crit Rev Biochem Mol Biol, 2020. **55**(2): p. 179-196.
34. Schafer, J.C., et al., *XBX-1 encodes a dynein light intermediate chain required for retrograde intraflagellar transport and cilia assembly in Caenorhabditis elegans.* Mol Biol Cell, 2003. **14**(5): p. 2057-70.
35. Hamada, Y., et al., *Interaction of WDR60 intermediate chain with TCTEX1D2 light chain of the dynein-2 complex is crucial for ciliary protein trafficking.* Mol Biol Cell, 2018. **29**(13): p. 1628-1639.
36. Tsurumi, Y., et al., *Interactions of the dynein-2 intermediate chain WDR34 with the light chains are required for ciliary retrograde protein trafficking.* Mol Biol Cell, 2019. **30**(5): p. 658-670.
37. Toropova, K., et al., *Structure of the dynein-2 complex and its assembly with intraflagellar transport trains.* Nat Struct Mol Biol, 2019. **26**(9): p. 823-829.
38. Yi, P., et al., *Dynein-Driven Retrograde Intraflagellar Transport Is Triphasic in C. elegans Sensory Cilia.* Curr Biol, 2017. **27**(10): p. 1448-1461 e7.
39. Asante, D., et al., *A role for the Golgi matrix protein giantin in ciliogenesis through control of the localization of dynein-2.* J Cell Sci, 2013. **126**(Pt 22): p. 5189-97.
40. Asante, D., N.L. Stevenson, and D.J. Stephens, *Subunit composition of the human cytoplasmic dynein-2 complex.* J Cell Sci, 2014. **127**(Pt 21): p. 4774-87.
41. Vuolo, L., et al., *Dynein-2 intermediate chains play crucial but distinct roles in primary cilia formation and function.* Elife, 2018. **7**.
42. Sulston, J.E., D.G. Albertson, and J.N. Thomson, *The Caenorhabditis elegans male: postembryonic development of nongonadal structures.* Dev Biol, 1980. **78**(2): p. 542-76.
43. Evans, J.E., et al., *Functional modulation of IFT kinesins extends the sensory repertoire of ciliated neurons in Caenorhabditis elegans.* J Cell Biol, 2006. **172**(5): p. 663-9.
44. Lanjuin, A. and P. Sengupta, *Specification of chemosensory neuron subtype identities in Caenorhabditis elegans.* Curr Opin Neurobiol, 2004. **14**(1): p. 22-30.
45. Hall, D.H. and R.L. Russell, *The posterior nervous system of the nematode Caenorhabditis elegans: serial reconstruction of identified neurons and complete pattern of synaptic interactions.* J Neurosci, 1991. **11**(1): p. 1-22.
46. MichaelsonL, *C. elegans: A Practical Approach.* Heredity, 2000. **213**.
47. Molin, L., et al., *Complexity of developmental control: analysis of embryonic cell lineage specification in Caenorhabditis elegans using pes-1 as an early marker.* Genetics, 1999. **151**(1): p. 131-41.
48. Altun, Z.F., Herndon, L.A., Wolkow, C.A., Crocker, C., Lints, R. and Hall, D.H. *WormAtlas*. 2002-2020.
49. Hu, P.J., *Dauer.* WormBook, 2007: p. 1-19.

50. Golden, J.W. and D.L. Riddle, *The Caenorhabditis elegans dauer larva: developmental effects of pheromone, food, and temperature.* Dev Biol, 1984. **102**(2): p. 368-78.
51. Hodgkin, J., *Male Phenotypes and Mating Efficiency in CAENORHABDITIS ELEGANS.* Genetics, 1983. **103**(1): p. 43-64.
52. Phillips, C.M., et al., *HIM-8 binds to the X chromosome pairing center and mediates chromosome-specific meiotic synapsis.* Cell, 2005. **123**(6): p. 1051-63.
53. Liu, K.S. and P.W. Sternberg, *Sensory regulation of male mating behavior in Caenorhabditis elegans.* Neuron, 1995. **14**(1): p. 79-89.
54. Taylor, S.P., et al., *Mutations in DYNC2LI1 disrupt cilia function and cause short rib polydactyly syndrome.* Nat Commun, 2015. **6**: p. 7092.
55. Reck, J., et al., *The role of the dynein light intermediate chain in retrograde IFT and flagellar function in Chlamydomonas.* Mol Biol Cell, 2016. **27**(15): p. 2404-22.
56. Li, W., P. Yi, and G. Ou, *Somatic CRISPR-Cas9-induced mutations reveal roles of embryonically essential dynein chains in Caenorhabditis elegans cilia.* J Cell Biol, 2015. **208**(6): p. 683-92.
57. Wingfield, J.L., et al., *IFT trains in different stages of assembly queue at the ciliary base for consecutive release into the cilium.* Elife, 2017. **6**.
58. Mijalkovic, J., et al., *Ensemble and single-molecule dynamics of IFT dynein in Caenorhabditis elegans cilia.* Nat Commun, 2017. **8**: p. 14591.
59. Prevo, B., et al., *Functional differentiation of cooperating kinesin-2 motors orchestrates cargo import and transport in C. elegans cilia.* Nat Cell Biol, 2015. **17**(12): p. 1536-45.